Optical generation of crystalline, quasicrystalline, and arbitrary arrays of torons in confined cholesteric liquid crystals for patterning of optical vortices in laser beams

Paul J. Ackerman, Zhiyuan Qi, and Ivan I. Smalyukh

Optical generation of crystalline, quasicrystalline, and arbitrary arrays of torons in confined cholesteric liquid crystals for patterning of optical vortices in laser beams

Paul J. Ackerman,[1,2] Zhiyuan Qi,[1] and Ivan I. Smalyukh[1,2,3*]

[1]Department of Physics, University of Colorado, Boulder, CO 80309, USA
[2]Department of Electrical, Computer, and Energy Engineering, Liquid Crystal Materials Research Center, and Materials Science and Engineering Program, University of Colorado, Boulder, CO 80309, USA
[3]Renewable and Sustainable Energy Institute, National Renewable Energy Laboratory and University of Colorado, Boulder, CO 80309, USA
[*]E-mail: ivan.smalyukh@colorado.edu .

Abstract

Condensed matter systems with topological defects in the ground states range from the Abrikosov phases in superconductors, to various blue phases and twist grain boundary phases in liquid crystals, and to phases of skyrmion lattices in chiral ferromagnets and Bose-Einstein condensates. In nematic and chiral nematic liquid crystals, which are true fluids with long-range orientational ordering of constituent molecules, point and line defects spontaneously occur as a result of symmetry-breaking phase transitions or due to flow, but they are unstable, hard to control, and typically annihilate with time. Here we describe optical generation of two-dimensional crystalline, quasicrystalline and arbitrary ensembles of particle-like structures manifesting both skyrmion-like and Hopf fibration features - dubbed "torons" [1] - comprised of looped double twist cylinders and point defects embedded in a uniform director field. In these two-dimensional lattices, we then introduce various dislocations, defects in positional ordering of the torons. We show that the periodic defect lattices with and without dislocation are light- and voltage-tunable reconfigurable two-dimensional diffraction gratings and can be used to generate various controlled phase singularities in the diffracted laser beams. The results of computer simulations of optical images, diffraction patterns, and phase distributions with optical vortices are in a good agreement with the corresponding experimental findings.

1. Introduction

Defects are fascinating objects commonly observed both in ordered or partially ordered condensed matter systems [1-19] and in the phase of light [20-33]. They have attracted a great deal of attention in different branches of science, ranging from condensed matter physics to cosmology in laboratory experiments [34,35]. Defects are typically found in the form of singular points, lines, or walls at which the orientational or translational positional order of structured materials, such as crystals or liquid crystals (LCs), is disrupted [2-4]. Although being important for understanding the physical underpinnings of many phenomena, defects were often treated as undesirable in applied research and technology [36-39]. For example, development of LC displays [36,37] and electro-optic devices based on crystals or LCs traditionally relied on the use of defect-free samples [3,36,38,39]. However, more recent developments in the field suggest a great potential for defect-enabled applications [1]. For example, Poulin *et al.* were the first to show that defects, along with the accompanying elastic distortions, enable novel long-range colloidal interactions in LC fluids that can be used in self-assembly of colloidal particles [40]. This discovery resulted in the current quest to develop a novel class of tunable LC colloidal composites based on self-assembly of nano - and microparticles with various types of surface treatment and shapes [41]. In a different recent development, cholesteric LC blue phases with periodic lattices of defect lines have emerged as novel functional materials for LC displays [42,43]; wide-temperature-range blue phase LCs now enable the new "blue phase" display mode with unprecedented refresh rate and superior characteristics (e.g., viewing angle) [42]. Defects are also important in other condensed matter systems. For example, in photonic crystals and photonic crystal fibers, deliberately introduced defects allow for a robust control of nearly lossless flow of light, control of mirrorless distributed feedback lasing, and a number of other exciting properties and applications [5]. Similar to the case of condensed matter systems, defects are abundant and play an important role in the fields of optics and photonics. For example, well-defined optical phase singularities, in which phase of light has a discontinuity, greatly enrich the properties of laser beams and find practical applications in a variety of novel methods of imaging, laser trapping, microfabrication, and telecommunications [20-22].

In liquid crystals, defects introduce well-defined spatial patterns of the LC director field $\mathbf{n(r)}$ (which is the coordinate-dependent optical axis for these uniaxial media and describes spatial variations of local average orientation of LC molecules) and corresponding patterns of

polarization-dependent effective refractive index [2,3]. However, appearance of these defects is poorly controlled and typically requires flow, high applied fields, or heating of the sample to the isotropic phase with subsequent quenching of temperature to bring the sample back to the LC phase [3,19]. Furthermore, defects commonly annihilate to minimize the elastic free energy of the LC [3]. Our previous studies have demonstrated that focused laser beams with optical phase singularities can be utilized to control topological defects in LCs through the optical generation of twist-bound ensembles of point and ring-shaped defects dubbed "torons" [1,44]. In this work, we describe optical patterning of defects in confined LCs to form two-dimensional crystalline lattices of torons with and without various types of dislocations and then use them to pattern dislocation defects in the optical phase and wavefront of laser beams. Using laser tweezers with computer-programmed steering of a focused laser beam, the electrically erasable long-term-stable periodic crystal lattices of torons are dynamically modified and tailored depending on the need, offering unprecedented means of control over phase singularities of the diffracted laser beams. These findings demonstrate a great potential for bridging fundamental studies and applications of defects in soft condensed matter, photonics, electro-optics, and other fields.

2. Materials and Techniques
2.1. Materials and sample preparation.
Our studies employ frustrated chiral nematic LCs (CNLCs) confined between glass plates with vertical surface boundary conditions. CNLC samples of desired cholesteric pitch p are formed by mixing nematic hosts such as 4-cyano-4'-pentylbiphenyl (5CB) or E7 (a commercial mixture of four different chemical compounds) with a chiral dopant 4-(2-methylbutyl)-4'-cyanobiphenyl (CB15) [1,44-46]. The used nematic LC hosts and chiral dopant were purchased from EM Chemicals and used as supplied. The value of the pitch $p = 1/(h_{HTP} \times C_{chiral})$ of CNLC of interest is selected by choosing an appropriate concentration C_{chiral} of the chiral dopant in the nematic host for the known value of the so-called "helical twisting power" h_{HTP} [1,44-46]. LC cells are fabricated using glass plates with transparent indium tin oxide (ITO) electrodes and alignment layers. Strong vertical surface alignment on the inner surfaces of the confining glass plates is set by treating these substrates with N,N-dimethyl-n-octadecyl-3-aminopropyltrimethoxysilyl chloride (DMOAP) by means of dip-coating in a 1wt% aqueous solution [1]. LC cells with the cell gap thickness $d = 5\text{-}30$ μm are produced by sandwiching glass

substrates interspaced by glass fiber segments of corresponding diameter. Thickness uniformity of the cell is characterized by observing interference of white light and determined using measurements of light transmission as a function of wavelength with a spectrometer [19]. In fabricated cells, d is typically set to be comparable to p, with d/p being within the range of 0.8-1. We infiltrate the LC into the cell by capillary forces at 85 °C (above the temperature of transition to the isotropic phase of used mixtures) to prevent flow related defects. We then seal the cell with epoxy. For electric control of the CNLC structures, wire leads are attached to the transparent conductive ITO coatings by using conductive tape and soldering.

2.2. Laser scanning setup for optical generation of toron arrays

We utilize a computer-controlled laser tweezers system based on a pair of scanning mirrors [19] that allows one to steer a laser beam between locations within the sample at which individual torons are generated via continuous tight focusing of the beam into the CNLC bulk for 15ms or more. The used experimental setup (Fig. 1) consists of a continuous wave (CW) Ytterbium-doped fiber laser (1064 nm, obtained from IPG Photonics) with collimated output beam diameter of 5 mm and a two-axis scanning mirror head XLRB2 (Nuttfield Technology) integrated with an upright polarizing optical microscope BX-51 (Olympus). The tweezers system is designed to enable computer-programmed steering of a focused beam between arbitrary sets of coordinates in the sample. The two scanned mirrors are powered by a digital-analog converter (NI PCI-MIO-16E-4, obtained from National Instruments) controlled by home-made Labview-based software. These mirrors enable voltage-controlled two-dimensional beam deflection and computer-programmed steering of the focused beam within the sample. The laser beam is first directed into the scanning head, reflected by its two mirrors, and then introduced into the microscope by means of a two-lens telescope with no magnification (Fig. 1). The telescope images the plane of scanning mirrors to the back aperture of the objective while also maintaining the collimation of the laser. Deflection angles defined by the scanning mirrors are converted into positions in the sample plane by the microscope objective. Using this setup and homemade Labview-based software, we generate large arrays of torons by fast sequential computer-programmed positioning of the focused beam in the sample locations at which we intend to generate torons. To assure reliable generation of toron patterns, the focused beam stays at the toron generation sites for 15ms or more and is scanned between the sites at rates of 1kHz and faster. In addition to optical

fields, low-frequency electric fields (1 kHz, up to 10 V_{p-p}) are applied to the CNLC cells using a DS345 generator (Stanford Research Systems) for electric control of structures, defects, and diffraction patterns.

2.3. Optical phase mapping setup and method

Phase mapping of diffracted laser beams is implemented using an approach described in details in Ref.[30] and an optical setup for the measurement of Stokes parameters shown in Fig. 2 [38,39]. In the setup, a Mach–Zehnder type interferometer is used to measure the relative phase shift between two collimated coherent beams of light. A 633nm He-Ne laser with beam diameter of 1mm is split into reference and probing beams by the beam splitter BS1. Both arms of the interferometer have an afocal lens pair for collimation of each beam independently. The reference beam is collimated by the lens pair L1 and L2 and then polarized horizontally by a polarizer P1. The probing beam is collimated by L3 and L4 as it is directed through the sample and then the diffracted beams of interest are selected by a mirror and polarized vertically by P2. The two collimated beams are then recombined by BS2 followed by a rotatable quarter wave plate and polarizer used for the measurement of the required intensities needed to determine the Stokes parameters. A camera (Nikon D300) is then used as an array detector to measure the intensity profile of the beam and controlled to assure that there is no overexposure such that its response scales linearly with intensity.

We measure four intensity profiles $I(\theta_{\lambda/4},\theta_P)$ for different azimuthal orientation angle combinations of the quarter-wave plate $\theta_{\lambda/4}$ and the polarizer θ_P in the Stokes polarimetry setup (Fig. 2). Phase reconstruction of selected diffraction orders of interest was performed using the method of Denisenko *et al.* described in Ref. [30] in which the Stokes parameters S_2 and S_3 are calculated using the measured intensities values as $S_2 = I(\pi/4,\pi/4) - I(3\pi/4,3\pi/4)$ and $S_3 = I(\pi/4,0) - I(3\pi/4,0)$ (Fig. 2). The coordinate-dependent relative phase shift between the co-located reference and probing beams in their lateral plane is then calculated as $\delta = \arctan(S_3/S_2)$ and visualized using Matlab software. The phase profiles $\delta(x,y)$ of the optical vortex beams are presented using both 2D and 3D representations and show discontinuous changes of phase at the location of optical vortices.

2.4. Imaging of generation dynamics and three-dimensional structure of toron arrays

The scanning-mirror laser tweezers system is integrated with an upright polarizing optical microscope (POM) BX-51 (from Olympus) used to image LC texture and dynamics of their evolution. In a typical experiment, the sample is placed between two crossed polarizers and viewed in a transmission-mode POM while the defect structures are being generated and manipulated via steering the focused beam. Imaging light traversing through the inter-toron homeotropic LC regions with vertical $\mathbf{n}(\mathbf{r})$ (along the microscope's axis) is blocked by the set of crossed polarizers as polarization of the light remains unchanged while propagating in the LC along vertical $\mathbf{n}(\mathbf{r})$. Cell regions with torons and various director distortions alter polarization of incoming linearly polarized imaging light due to the in-plane component of $\mathbf{n}(\mathbf{r})$ (Fig. 3). Laser generation of structures and their imaging with POM are implemented by use of a broad range of microscope objectives with 10x-100x magnification and numerical apertures (NA) within NA=0.1-1.4, depending on the need.

Director structures in the vertical cross-sections of the LC cells are studied using the three-photon excitation fluorescence polarizing microscopy (3PEF-PM). This technique is an imaging modality of the nonlinear optical polarizing microscopy described in details in Ref. [47]. A tunable, pulsed Ti:sapphire oscillator with 140 fs pulse durations at an 80 MHz repetition rate (Coherent Chameleon Ultra-II) is employed as an excitation source for the 3PEF-PM. The oscillator output can be tuned over a 680-1080 nm wavelength range to optimize the three-photon absorption excitation of used CNLC materials. To control the linear polarization state, the beam is passed through a Glan-Thompson polarizer and a rotatable half-wave plate. This beam is then directed into the laser scanning head (Olympus FV-300) integrated with an inverted optical microscope IX-81 (Olympus). A 100x objective with high NA=1.4 focuses the beam to a diffraction-limited spot while a pair of galvano mirrors within the scanning head steers the spot within the focal plane of the objective. A stepper motor controls the height of the objective so that 3D images can be assembled by software from a series of 2D optical scans obtained at different depths of the sample. Since the laser excitation intensities needed to induce significant three-photon absorption only exist within a small volume around the focal point of the microscope objective, this approach provides an intrinsic diffraction-limited 3D optical imaging resolution. We use a beam at 870 nm wavelength to excite the molecules of used CNLCs directly via the three-photon absorption process and detect the emitted fluorescence signal in an epi-

detection scheme using a bandpass filter centered at 417 nm (bandwidth 60 nm) and a photomultiplier tube (PMT). Since the transition dipole moments of multi-photon absorption and fluorescence are aligned with the long axes of LC molecules, polarized multiphoton excitation and unpolarized detection yield fluorescence textures with strong signal intensity dependence on spatial changes of long-range molecular orientation patterns. The intensity scales as $\cos^6\phi$, where ϕ is the angle between $\mathbf{n}(\mathbf{r})$ and the used linear polarization direction of laser light [47]. Fluorescence textures obtained for different sample cross-sections and different 3PEF-PM imaging polarizations allow one to reconstruct the studied 3D $\mathbf{n}(\mathbf{r})$-fields of laser-generated structures (Fig. 4), as discussed in details below.

3. Computer simulations of POM and 3PEF-PM textures and diffraction patterns

By taking the computer-simulated 3D director structure (obtained in our previous studies [1] by means of numerical minimization of elastic free energy using the director relaxation method) of an individual toron as a building block of studied laser-generated defect arrays (Fig. 3B,D), we have simulated the corresponding POM textures using the extended Jones matrix method [36]. These simulations utilize experimental material and sample parameters (such as optical anisotropy, pitch, and cell thickness). To simulate a POM texture, an LC sample with a toron surrounded by homeotropic uniform $\mathbf{n}(\mathbf{r})$ was split into a set of thin slabs with known director orientation patterns given by the numerical modeling. While traversing through the cell, light splits into ordinary and extraordinary waves that have electric fields perpendicular and parallel to the in-plane projection of $\mathbf{n}(\mathbf{r})$, respectively. These waves "see" ordinary refractive index $\mathbf{n_o}$ and an effective extraordinary refractive index $n_{ee}(\theta)$ dependent on θ between $\mathbf{n}(\mathbf{r})$ and the light's propagation direction, respectively [3,36]. The effect of each thin slab is equivalent to that of a phase retardation plate with spatially varying optical axis in the lateral plane but constant orientation of the optical axis across its thickness and can be described by a coordinate-dependent Jones matrix [36]. In each pixel of a simulated POM texture, intensity of the light after propagation through the cell is obtained by successive multiplication of the Jones matrices corresponding to a polarizer, a series of thin nematic slabs with coordinate-dependent phase retardation, and an analyzer. To mimic the achromatic-light observations in our POM experiments, we have performed these calculations for wavelength 475 nm, 510 nm, and 650 nm

and then superimposed the resulting textures to obtain a POM image for white imaging light. In addition to POM images, we also simulate 3PEF-PM images by first calculating the angle ϕ between $\mathbf{n(r)}$ and the linear polarization direction of the used excitation laser light and then evaluating the 3D normalized fluorescence intensity patterns as $\cos^6\phi(\mathbf{r})$. We find that the computer-simulated POM images (Fig. 3) and 3PEF-PM images in 3D Paraview presentation (Fig. 4C,D) closely match the corresponding experimental results; this type of visualization of complex director fields will be discussed in further details elsewhere [48].

We also use the minimum-energy simulated $\mathbf{n(r)}$-structure of the toron to model the phase distribution of a beam passing through multiple torons that serve as "building blocks" of studied phase diffraction gratings. Similar to the case of POM texture simulations, the LC sample with a grid of patterned toron structures is again split into a similar set of thin slabs with a known orientation of $\mathbf{n(r)}$ and described by a similar set of Jones matrices. The ordinary and extraordinary waves experience different phase gain while propagating through each of the thin LC slabs. The lateral phase distribution of linearly polarized incident light after propagation through the cell is obtained by successive multiplication of the Jones matrices corresponding to the series of thin sample slabs acting as phase retardation plates with known spatial patterns of the optical axis orientation. This yields a coordinate-dependent phase distribution of the light after exiting the sample. The resulting near-field phase profile experienced by the laser beam due to torons is then used to calculate the far-field diffraction pattern. In order to obtain light intensity distributions in the far-field, we multiply the calculated phase distribution by a Hamming function to approximate the Gaussian profile of a laser beam and then propagate the beam to the far-field using the Fraunhofer equation [38,39].

4. Laser-generated voltage-tunable two-dimensional crystals of torons

The used CNLCs have twisted ground-state configuration of $\mathbf{n(r)}$ which is characterized by cholesteric pitch p, a distance along the helical axis over which mesogenic molecules and $\mathbf{n(r)}$ rotate by 2π. Despite of the preference to form one-dimensional twisted structures, CNLCs can be untwisted by external fields and/or confinement into thin cells. For example, in the studied LC cells with vertical boundary conditions for $\mathbf{n(r)}$ and of thickness d about equal or smaller than the equilibrium cholesteric pitch p, one typically observes a fully unwound frustrated state with a uniform vertical $\mathbf{n(r)}$. The CNLC's tendency to form twisted structures is suppressed in this case.

By focusing a Gaussian laser beam into these cells (Fig. 1), we generate the so-called triple-twisted torons of the first kind [1] (referred to simply as "torons" in this article) containing two point singularities and a ring of twist-escaped disclination (Fig. 4A,B), as reconstructed using 3PEF-PM and conventional POM images (Figs. 3A,C and 4D). In the process of generation, the focused laser beam of sufficient power initially causes rotation of the director field away from the vertical orientation and then spontaneous formation of the complex toron structure (stable even after turning off the beam) that corresponds to global or local minimum of the elastic free energy [1]. The appearance of torons under crossed polarizers in POM depends on the birefringence of LC, toron size, and sample thickness, however, as these parameters are varied, computer-simulated POM and 3PEF-PM textures always match the corresponding experimental counterparts (Fig. 3 and Fig. 4C,D) [1]. Rather unexpectedly, the defects comprising torons do not annihilate or repel apart. In contrast, these defects are bound to each other at a certain well-defined distance by the inter-defect regions of the sample with twisted $\mathbf{n(r)}$ that help to minimize elastic energy cost of the entire structure. The twist-interspaced point and line defects form stable or metastable 3D configurations, depending on LC material properties and the d/p ratio [1]. In the confinement-unwound cholesteric LC cells with vertical boundary conditions, these laser-generated topological defects embed the localized twist of $\mathbf{n(r)}$ into the uniform background director field, forming distinct localized elastic particle-like excitations (Fig. 4) [1].

The long-term stability of various 2D arrays of torons can be understood by analyzing elastic free energy and comparing it to that of a homeotropic texture of the surrounding confinement-unwound CNLC [2,3,49]. The elastic free energy density reads:

$$f_{elastic} = \frac{K_{11}}{2}(\nabla \cdot \mathbf{n})^2 + \frac{K_{22}}{2}[\mathbf{n} \cdot (\nabla \times \mathbf{n}) + \frac{2\pi}{p}]^2 + \frac{K_{33}}{2}[\mathbf{n} \times (\nabla \times \mathbf{n})]^2 - \\ K_{24}\{\nabla \cdot [\mathbf{n}(\nabla \times \mathbf{n}) + \hat{n} \times (\nabla \times \mathbf{n})]\}, \tag{1}$$

where K_{11}, K_{22}, K_{33}, and K_{24} are Frank elastic constants for splay, twist, bend and saddle splay deformations, respectively. Similar to the case of individual laser-generated torons [1], their arrays minimize twist and saddle splay terms of Eq. (1). However, this is at the expense of elastic free energy cost of additional bend and splay distortions (first and third terms in the above equation) as well as core energies of point defects within the toron structures. Although the homeotropic uniform structure with or without individual torons as well as periodic arrays of torons interspaced by the homeotropic texture have comparable free energies per unit area of the

cell, strong elastic energy barriers associated with the transformation of a toron into homeotropic texture or vice-versa preclude spontaneous transitions between these stable/metastable states while allowing one to induce these transitions by applied fields and laser beams.

The studied here triple twisted torons of the first kind are each comprised of two hyperbolic point defects and twist-escaped integer-strength disclination loops embedded into the uniform vertical director field (Fig. 4) [1]. Mapping of the director field around the point defects onto the order parameter space (two-sphere S^2/Z_2 with pairs of diametrically opposite points being identical) shows that both of them have elementary charge with the absolute value of unity (Fig. 4A). Since the nematic director has non-polar symmetry, the assignment of the signs to these defects depends on a convention as different approaches have been introduced in the past to determine the sign of topological hedgehog charges [1-5]. Following the traditionally used convention [3-5], the hyperbolic point defects (Fig. 4A,B) and disclination loops of strength s=-1/2 were commonly assigned topological charge of "-1" while radial point defects and s=1/2 disclination loops were commonly assigned hedgehog charge "+1". In analogy, following this convention, a loop of an integer-strength disclination s=1 can be assigned a hedgehog charge of "+2", compensating the two "-1" point defect charges and providing one way of understanding the topological charge conservation in the toron structure with two hyperbolic point defects and a looped double-twist cylinder treated as a loop of twist-escaped disclination (Fig. 4A,B) [1]. A different approach of assigning signs of point defects and disclination loops, recently discussed in Ref. [14], requires having a global point of reference and the use of vector field lines in the nematic or cholesteric texture until the signs of the hedgehog charges are assigned with respect to this global reference point (Fig. 4E). Assignment of charges of topological point defects then depends on the direction of vector field lines at the global point of reference and can be reversed by flipping this direction to an opposite one. Using this approach, one can assign opposite signs of hedgehog charges to the two point defects within the toron and mapping of the texture of looped double-twist cylinder onto the corresponding two-sphere order parameter space yields a net hedgehog charge equal to zero (Fig. 4E). Having two point defects of opposite topological hedgehog charge then again assures that the total topological charge is equal to zero (conserved), regardles of the choice of the global reference point and vector field direction that only determine which of the two point defects is "-1" and which is "+1". Interestingly, the uniformly twisted director field lines on a family of nested tori of the toron structure (Fig. 4A) resemble the

stereographic projection of the Hopf fibration [1] localized in a finite-volume of the cell with vertical boundary conditions by means of the hyperbolic point defects.

The studied torons can be optically generated at a desired location in the sample. Using a scanning laser generation system (Fig. 1), one can program a focused laser beam to visit arbitrary locations in the confined CNLC sample and, for example, generate individual torons shown in Figs. 3 or periodic lattices formed by them (Fig. 5A,B). In flat LC cells with strong surface anchoring and thickness about 5 μm and larger as well as lateral sample thickness variations of about 1% or less, torons generated by laser beams of power of 50mW and higher are typically immobile and can be used to form long-term stable two-dimensional lattices such as the ones shown in Fig. 5A,B. Since director twist is of benefit from the elastic energy standpoint only if it occurs with effective pitch equal or close to the equilibrium pitch p, torons strongly repel from each other at small center-to-center separations smaller than p. They weakly repel at somewhat larger distances of (1-1.4)p to minimize elastic free energy due to convex-type distortions of $\mathbf{n(r)}$ at the toron's periphery and overall decrease of distortions and elastic energy cost as the inter-toron distance increases. However, these repulsive interactions quickly vanish with distance and are comparable or smaller than k_BT at distances of 1.5p and larger. Although torons of small size (e.g. equal or smaller than one micrometer) can undergo Brownian motion within the LC cell, the use of generating laser powers of 50-150mW assures that they are strongly pinned in the location at which they have been generated. This pinning is likely due to minor laser-induced perturbations in the surface alignment provided by the surfactant monolayer coatings of the substrates, so that periodic lattices of torons can remain intact over long periods of time (Fig. 5A,B). The combination of surface pinning with the absence of strong interactions at relatively small inter-toron distances of 1.5p and larger allows one to optically generate a number of patterns formed by torons, such as periodic crystalline lattices shown in Fig. 5(A,B). Mobile torons (not pinned to the original generation locations) act as particle-like structures and can also assemble into hexagonal crystalline structures by exploiting lateral confinement and the short-range repulsive interactions; however, their Brownian motion, interactions, and self-assembly go beyond the scope of the present work and will be explored in details elsewhere [50].

5. Arrays of torons as phase gratings

Square-periodic and hexagonal lattices of torons can be used as two-dimensional phase

diffraction gratings, yielding diffraction patterns (insets of Figs. 5A,B, 6, and 7) that indicate highly periodic organization of torons in the LC sample. Since the LC's effective refractive index depends on the light's polarization and propagation directions with respect to $\mathbf{n(r)}$, the arrays of torons yield periodic patterns of effective refractive index and result in phase gratings obtained by means of laser-guided structural self-assembly. Using the superposition of equilibrium $\mathbf{n(r)}$-structure of individual torons (obtained via minimization of the elastic free energy [1]), we have composed $\mathbf{n(r)}$ of square-periodic and hexagonal lattices of torons mimicking the experimental lattices shown in Fig. 5A,B and calculated the ensuing periodic refractive index patterns for circularly polarized incident light. We then used thus obtained refractive index and phase distributions to computer-simulate the diffraction patterns in the far field (as described in the section 3 above) and find them being in agreement with experimental results (compare patterns shown in Fig. 8 to the experimental ones shown in Figs. 5, 6 and 7).

The obtained 2D diffraction patterns satisfy the well-known condition for maximum intensity, $(m_x^2 + m_y^2)^{1/2}\lambda = L_{tg} \sin \theta$, and have intensity maxima at distances r from the center of 0-th order beam given by $r = \lambda D(m_x^2 + m_y^2)^{1/2}/ L_{tg}$, where λ is the wavelength of laser light used to obtain diffraction patterns, θ is the diffraction angle, L_{tg} is the toron grating periodicity, D is the distance from the grating to the screen, and m_x and m_y are the diffraction orders in the x and y directions, respectively [38]. Intensities of different diffraction orders can be continuously tuned by applying voltage (Figs. 5-7), until the diffraction grating of torons is fully erased at modestly strong electric fields (supplementary video 1 [58]). This electric control is possible because of the free energy term describing coupling between $\mathbf{n(r)}$ and electric field $\mathbf{E}$ due to voltage applied between the transparent electrodes of the LC cell. The effects of low-frequency AC electric field $\mathbf{E}$ due to the voltage applied to cell's transparent electrodes can be explained by minimization of the electric field term of the free energy density $f_{electric} = -\dfrac{\varepsilon_0}{2}\Delta\varepsilon(\mathbf{E} \cdot \mathbf{n})^2$, where ε_0 is vacuum permittivity and $\Delta\varepsilon$ is the dielectric anisotropy that can be positive or negative, depending on the used material [3,36].

In studied LCs with positive dielectric anisotropy, such as the CNLC mixtures based on 5CB and E7, coupling with an electric field causes rotation of $\mathbf{n(r)}$ toward the cell normal (i.e., toward $\mathbf{E}$) and allows one to tune size and internal structure of torons in the lattice. As applied voltage gradually increases, the refractive index contrast between the torons and their

homeotropic surrounding decreases (Fig. 5C,D). This continuous control of ensuing 2D patterns of effective refractive index allows for the control of the diffraction pattern. Furthermore, at relatively high applied voltages of about $2V_{p-p}$ and higher, the gratings of torons can be fully erased by the field as individual torons disappear due to unwinding of $\mathbf{n(r)}$ (Figs. 6 and 7 and supplementary video 1), which can be followed by generation of a new array/grating by scanning of the laser beam. Thus, facile laser generation of torons by scanned laser beams and electric control of these structures provide a new type of optically reconfigurable voltage-tunable phase diffraction grating of interest for many applications.

The axially symmetric director configuration of an individual toron yields polarization-dependent refractive index pattern and also polarization-sensitive phase gratings. Most of the diffraction grating data presented in this work have been obtained for circularly polarized probing light. For linearly polarized incoming laser light, diffraction patterns show strong dependence on orientation of the linear polarization with respect to the crystallographic axes of the crystalline arrays of torons, as shown in the supplementary videos 2 and 3 using examples of square-periodic and hexagonal gratings.

6. Generation of phase singularities in diffracted laser beams

Facile optical generation of arbitrary reconfigurable 2D patterns of torons makes our system ideal for probing how defects in the crystal-like gratings can induce and control defects in the optical phase of diffracted laser beams. To study phase profiles of diffracted laser beams, we use the Stokes polarimetry setup shown in Fig. 2 and the method described in the section 2.3 above [30,32]. We probe phase profiles of beams in diffraction patterns due to gratings with various dislocations and other defects in periodic crystalline arrays of torons, which we generate by electrically (via applying voltage to the transparent electrodes) erasing and then optically recreating the desired toron arrays (Figs. 9-11).

An optically generated square-periodic 2D phase grating of torons with an elementary edge dislocation (Fig. 9A) yields a 2D diffraction pattern shown in Fig. 9B. The diffracted beams with $m_y=0$ have Gaussian-like intensity distributions but the beams with $|m_y| \geq 1$ contain one or more low-intensity spots in their intensity profiles. Mapping of lateral phase dustributions reveals no singularities in beams with $m_y=0$ and presence of phase singularities in all beams with $|m_y| \geq 1$. As an example, this is demonstrated for the case of the diffracted beam $m_x=0$, $m_y=1$ in

Fig. 9(C-I) and for the beam m_x=0, m_y=2 in Fig. 9(F-J). A hexagonal grating with the so-called 5-7 point defect dipole in the hexagonal lattice shown in Fig. 10(A,B) also yields a pattern with phase singularities in diffracted beams shown in Fig. 10C-E (note that the 5-7 dipole can be also viewed as a set of two edge dislocations in the hexagonal lattice inserted along two different crystallographic axes) [2]. Similarly, a square periodic pattern of torons with a set of two orthogonal elementary edge dislocation defects in the center of the toron array shown in Fig. 11(A) yields a diffraction pattern shown in its inset of Fig. 11(A), with the diffracted beams having phase singularities characterized in Fig. 11(B-E). The details of phase distributions of diffracted laser beams are visualized by means of two different representations and show that the phase varies continuously everywhere in the beam's lateral plane except for the locations of the screw dislocations (i.e., phase singularities), at which phase is undefined. The computer simulated laser intensity distributions in the diffraction patterns and the phase profiles (Fig. 11F-H and Fig. 12) are in a qualitative agreement with the corresponding experimental results (Fig. 11A-E, 9 and 10).

Characterization of phase profiles of laser beams in different diffraction orders of square-periodic gratings with dislocation defects (Figs. 9 and 11-13) reveals a simple relation between their total topological charge $N(m_x, m_y)$ (here N defines the number of twists the phase of the light makes in one wavelength and the sign of N defines the twist direction) of optical phase singularities in a diffracted beam of given order of interest and the Burgers vector $\mathbf{b}$ of the dislocation (perpendicular to the inserted new row of torons) in the diffraction grating: $N(m_x, m_y) = \pm(b_x|m_x| + b_y|m_y|)/a$, where a is the lattice periodicity; this result is consistent with previous studies of other types of gratings with defects [30-33]. For example, since the grating with a dislocation shown in Fig. 9a has b_x=0 and b_y=a, the combined charge of all phase singularities in diffraction orders $N(m_x, 0) = 0$, $N(m_x, \pm 1) = \pm 1$, $N(m_x, \pm 2) = \pm 2$, and so on.

A good qualitative agreement between simulated and experimental phase profiles (Figs. 11 and 12 and Supplementary Fig. S1) shows that patterning of defects in toron gratings can reliably control phase singularities in diffracted laser beams. Similar to the case of high-strength disclinations and high-charge point defects in nematic LCs, which are known to split into defects of lower charge to minimize elastic energy [3], the phase singularities of large N also tend to split into multiple phase singularities of elementary charge $N = \pm 1$ (Fig. 9B,F-J). The physical

underpinnings of this splitting are different as compared to defect splitting in LCs. The splitting of high-charge phase singularities into the elementary ones is usually attributed to inherent presence or addition of small coherent background in a screw-dislocated wave of the laser beam [31-33]. The demonstrated voltage tunability of the diffraction patterns provides unprecedented means of tuning both intensity and phase distributions in the diffraction patterns (Fig. 13), similar to the case of dislocation-free arrays discussed in the previous section.

7. Toward a model system for probing the interplay of defects in condensed matter and in electromagnetic waves

In conventional atomic, molecular or colloidal crystals with long-range positional order, dislocations and disclinations are sources of mechanical stress and therefore energetically costly. Therefore, only a limited combination of these defects in such condensed matter systems can spontaneously occur or be induced by external fields [4]. Furthermore, probing the effect of individual defects in, say, atomic or molecular systems on phase of electromagnetic waves would require detailed characterization of phase of diffracted x-ray and electron beams with wavelength comparable to crystal periodicity, which is typically impractical. In colloidal systems and various LCs with partial long-range or quasi-long-range positional ordering (e.g. smectic and columnar LCs), defects such as dislocations also correspond to short-lived metastable states (unless the crystals with defects occur on curved surfaces so that this stress is relieved by curvature [2, 25]) and only limited types of defects can be obtained. These constraints are not present in our model system because interactions between the surface-pinned torons are negligible and there is no significant energy cost due to introducing various defects into the arrays of torons which can be generated by simply scanning the laser beam and "drawing" desired arrays/patterns. Thus, our system offers a means for probing the interplay of defects in soft condensed matter and optics, which can potentially yield a number of general conclusions important for the study of defects in different fields. Furthermore, homeotropic CNLC cells with torons allow for the generation of structures rather uncommon for two-dimensional colloidal and molecular systems, such as the honeycomb lattice (Fig. 14A), a square-periodic lattice with a bifurcated homeotropic channel formed by missing rows of torons (Fig. 14B), and various quasicrystal-like structures (Fig. 15) [51]. Thus, laser-generated patterns of torons offer a testbed for probing various theoretical predictions and also for facile experimental exploration of interaction of laser beams and various

unconventional phase diffraction gratings with optically controlled singularities and quasicrystalline or partial order.

An interesting property of the studied system is that it contains defects at different levels (i.e., the torons comprise twist-bound line and point defects in molecular ordering and in twist directionality that then are used to form defect arrays with dislocations, defects in the periodic arrangements of these elastic quasiparticles). We have previously shown that the types and organization of defects within torons can be controlled by introducing defects into phase of the generating laser beams [1]. The present work, in turn, demonstrates that dislocation defects in the arrays of torons used as diffraction gratings allow for the control of optical phase singularities in the diffracted laser beams. In addition to the torons of the first kind used as a building block of periodic lattices in this work, one can compose phase gratings from torons having other defect structures (e.g. with half-integer disclination loops instead of point defects comprising the structure shown in Fig. 4A [1]), cholesteric fingers of different kinds [45, 46, 52], as well as mixed structures containing torons and fingers of different kinds [53, 44]. This unprecedented control over spatial organization of defects in gratings may offer a wide range of applications, such as optical data storage [37], light/voltage controlled information displays [36], tunable photonic crystals [37], light-controlled LC elastomers [54], defect-mediated organization of metal and semiconductor nanoparticles in LCs [55, 56], etc.

8. Conclusions

We have demonstrated that laser-guided self-assembly of periodic arrays of localized structures - dubbed torons - allows for facile generation of reconfigurable and tunable phase diffraction gratings with and without dislocation defects as well as in the form of quasicrystal-like patterns. The key advantage of the demonstrated optically- and electrically-reconfigurable diffraction gratings over their micro-fabricated counterparts and electrically addressed spatial light modulators (typically used to generate phase singularities in the laser beams) is the robustness with which the periodic patterns of liquid crystal defects can be generated and switched between multiple distinct long-term-stable states. Since the lattice periodicity of optically induced structures depends on the equilibrium pitch of the used chiral nematic liquid crystal and can be tuned from several hundreds of nanometers to hundreds of microns by varying the pitch and utilizing different structure generation schemes, thus obtained diffraction gratings

can be designed to work in both Raman-Nath and Bragg regimes [38, 57, 58]. Structural multistability as well as low-voltage and low-laser-power switching may additionally lead to powerless and low-power multi-modal operation of electro-optic, photonic, and all-optical devices as well as new types of information display.

Acknowledgements

References

1. I.I. Smalyukh, Y. Lansac, N. Clark, R. Trivedi. *Nature Mater.* **9**, 139 (2010).

2. P. M. Chaikin and T. C. Lubensky, *Principles of Condensed Matter Physics* (Cambridge Univ. Press, 2000).

3. P.-G. de Gennes and J. Prost, *The Physics of Liquid Crystals* (Clarendon, Oxford, 1993), 2nd Ed.

4. M. Kleman, *Points, Lines and Walls* (Wiley, New York, 1983)

5. M. Kleman and O.D. Lavrentovich, Phil. Mag. **86**, 1-11 (2006).

6. C.H. Sun and P. Jiang. *Nature Photon.* **2**, 9-11 (2008).

7. K. Ishizaki and S. Noda. *Nature* **460**, 367-370 (2009).

8. R.P. Trivedi, I.I. Klevets, B.I. Senyuk, T. Lee, and I.I. Smalyukh, *Procs. Nat. Acad. Sci. U.S.A.* **109**, 4744-4749 (2012).

9. V. J. Anderson, H. N. Lekkerkerker. *Nature* **416**, 811-815 (2002).

10. P. Schall, I. Cohen, D. A. Weitz, F. Spaepen, *Science* **305**, 1944-1948 (2004).

11. A. M. Alsayed, M. F. Islam, J. Zhang, P. J. Collings, A. G. Yodh. *Science* **309**, 1207-1210 (2005).

12. M. Zapotocky, L. Ramos, P. Poulin, T. C. Lubensky, D. A. Weitz. *Science* **283**, 209-212 (1999).

13. L. Ramos, M. Zapotocky, T. C. Lubensky, D. A. Weitz. *Phys. Rev. E* **66**, 031711 (2002).

14. G.P. Alexander, B.G. Chen, E.A. Matsumoto, and R.D. Kamien, *Rev. Mod. Phys.* **84**, 497-514 (2012).

15. M. Skarabot, M. Ravnik, S. Zumer, U. Tkalec, I. Poberaj, D. Babic, I. Musevic. *Phys Rev E* **77**, 061706 (2008).

16. Y. Iwashita, H. Tanaka. *Phys. Rev. Lett.* **90**, 045501 (2003).

17. M. Ravnik, G. P. Alexaner, J. M. Yeomans, S. Zumer. *Faraday Discussions* **144**, 159-169 (2010).

18. N. Hijnen, T. A. Wood, D. Wilson, P. S. Clegg. *Langmuir* **26**, 13502-13510 (2010).

19. I. I. Smalyukh, D. S. Kaputa, A. V. Kachynski, A. N. Kuzmin, P. N. Prasad. *Opt Exp* **15**, 4359-4371 (2007).

20. L. Allen, M. W. Beijersbergen, R. J. C. Spreeuw, J. P. Woerdman. *Phys. Rev.* A **45**, 8185-8189 (1992).

21. J. Leach, M. R. Dennis, J. Courtial, M. J. Padgett. *New J. Phys.* **7**, 1-11 (2005).

22. J. Leach, M. R. Dennis, J. Courtial, M. J. Padgett. *Nature* **432**, 165 (2004).

23. M. Uchida, A. Tonomura. *Nature* **464**, 737-739 (2010).

24. S. Muhlbauer et al. *Science* **323**, 915-919 (2009).

25. W. T. M. Irvine, V. Vitelli, P. M. Chaikin. *Nature* **468**, 947-951 (2010).

26. J. Verbeeck, Tian, P. Schattschneider. *Nature* **467**, 301-304 (2010).

27. R. M. Dennis, R. P. King, B. Jack, K. O'Holleran, M. J. Padgett. *Nature Phys.* **6**, 118-121 (2010).

28. T. Lopez-Leon, V. Koning, K. B. S. Devaiah, V. Vitelli, A. Ferandez-Nieves. *Nature Phys.* **7**, 391-394 (2011).

29. W. T. M. Irvine, D. Bouwmeester. *Nature Phys.* **4**, 716-720 (2008).

30. V. G. Denisenko, A. Minovich, A. S. Desyatnikov, W. Krolikowski, M. S. Soskin, Y. S. Kivshar. *Opt. Lett.* **33**, 89-91 (2008).

31. M. S. Soskin, M. V. Vasnetsov. *Progress in Optics* **42**, 219-276 (2001).

32. I. V. Basistiy, V. Bazhenov, Yu., M. S. Soskin, M. V. Vasnetsov. *Optics Comm.* **103**, 422-428 (1993).

33. J. F. Nye, M. V. Berry. *Proc. R. Soc. Lond.* A **336**, 165-190 (1974).

34. I. Chuang, R. Durrer, N. Turok, B. Yurke. *Science* **251**, 1336 (1991).

35. R. Mosseri. *C. R. Chimie* **11**, 192-197 (2008).

36. P. Yeh, C. Gu, *Optics of Liquid Crystal Displays* (John Wiley & Sons, Inc., 1999).

37. S. J. Woltman, D. G. Jay, G. P. Crawford, *Nature Mater.* **6**, 929-938 (2007).

38. M. Born, E. Wolf, *Principles of Optics.* (Pergamon Press, 1975).

39. D. Clarke, J. F. Grainer, *Polarized light and optical measurement.* (Pergamon Press, 1971).

40. P. Poulin, S. Holger, T. C. Lubensky, D. A. Weitz, *Science* **275**, 1770-1773 (1997).

41. C. P. Lapointe, T. G. Mason, I. I. Smalyukh, *Science* **326**, 1083-1086 (2009).

42. L.-W. Liu, Q.-H. Wang, J.-P. Cui, *J. of the Society for Information Display* **19**, 547-550 (2011).

43. H. J. Coles, M. N. Pivnenko, *Nature* **436**, 997-1000 (2005).

44. O. Trushkevych, P. Ackerman, W. A. Crossland, and I. I. Smalyukh, *Appl. Phys. Lett.* **97**, 201906 (2010).

45. I. I. Smalyukh et al., *Phys. Rev. E* **72**, 061707 (2005).

46. P. Oswald, J. Baudry, S. Pirkl, *Physics Reports* **337**, 67-96 (2000).

47. T. Lee, R. P. Trivedi, I. I. Smalyukh, *Opt. Lett.* **35**, 3447-3449 (2010).

48. B. G. Chen, P. Ackerman, G. P. Alexander, R. D. Kamien, and I. I. Smalyukh, in preparation (2012).

49. R. D. Polak, G. P. Crawford, B. C. Costival, J. W. Doane, S. Zumer, *Phys. Rev. E* **49**, R978 (1994).

50. P. Ackerman, Y. Lansac, Z. Qi, and I. I. Smalyukh, in preparation (2012).

51. J. Mikhael, J. Roth, L. Helden, and C. Bechinger, *Nature* **454**, 501-504 (2008).

52. P. Ackerman, Z. Qi, Y. Lin, M. Juanes Laviada, I. I. Smalyukh, *Sci. Rep.* **2**, 414 (2012).

53. I. I. Smalyukh, D. Kaputa, A. V. Kachynski, A. N. Kuzmin, P. J. Ackerman, C. W. Twombly, T. Lee, R. P. Trivedi, P. N. Prasad, *Opt. Express* **20**, 6870-6880 (2012).

54. C. L. van Oosten, C. W. M. Baastiansen, D. J. Broer, *Nature Mater.* **8**, 677-682 (2009).

55. B. Senyuk, J. S. Evans, P. Ackerman, T. Lee, P. Manna, L. Vigderman, E.R. Zubarev, J. van de Lagemaat, I. I. Smalyukh, *Nano Lett* **12**, 955-963 (2012).

56. D. Engström, R.P. Trivedi, M. Persson, K.A. Bertness, M. Goksör, and I.I. Smalyukh, *Soft Matter* **7**, 6304-6312 (2011).

57. B. I. Senyuk, I. I. Smalyukh, O. D. Lavrentovich, *Opt. Lett.* **30**, 349-351 (2005).

58. See Supplemental Material at [URL will be inserted by publisher] for three videos showing how laser diffraction patterns obtained by use of toron arrays can be controlled via varying applied voltage and by means of changing polarization of incident laser light. The supplementary Figure S1 provides additional details on experimental studies and computer simulations of phase singularities produced by a hexagonal array of torons with 5-7 defects in the hexagonal ordering.

Figures Captions

Fig. 1. (Color online). Scanning-mirror laser tweezers setup used to generate 2D patterns of torons. The continuous wave (CW) collimated ytterbium fiber laser is controlled with a pair of scanning mirrors. Lenses L1 and L2 in a 4f configuration direct the beam into the back aperture of an objective. The scanning mirror angles determine the 2D positions of the focused beam within the sample. The dichroic mirror (DM) allows for simultaneous laser scanning for generation of torons and POM studies of the optically controlled samples. The crossed polarizer and analyzer are used to obtain POM textures.

Fig. 2. (Color online). Stokes polarimetry phase characterization setup used to map the phase of diffracted laser light. A Mach–Zehnder type interferometer is implemented by dividing a He-Ne laser beam into two paths and then recombining these two beams by beam splitters BS1 and BS2, respectively. The block and iris allow for selecting the diffraction order of interest. M1-M3 are silver mirrors used for redirecting the beam. The polarization of the beam is controlled by polarizers P1-P3 and the $\lambda/4$ plate. The beam is collimated by the use of lens pairs L1-L2 and L3-L4.

Fig. 3. (Color online). Experimental and computer-simulated POM textures of torons. (A,C) Experimental and (B,D) corresponding computer-simulated POM textures of laser generated torons of different size in a (A,B) 9μm-thick cell with CNLC pitch of about 10 μm and (C,D) 3.5μm-thick sample with pitch of about 5 μm. The used CNLC materials were mixtures of the nematic host E7 and chiral dopant CB15 at concentrations corresponding to pitch values of 5 μm

and 10 μm. In computer simulations, we utilized values of ordinary refractive index n_o=1.5, extraordinary refractive index n_e=1.7, and optical anisotropy $\Delta n = 0.2$, closely matching that of the used LC mixtures. The crossed polarizer and analyzer are shown by white double arrows and marked by "P" and "A", respectively.

Fig. 4. (Color online). Laser-generated torons in a confined CNLC. (A) Schematic of a toron **n(r)** configuration consisting of two hyperbolic point defects (blue dots on the top and bottom of the schematic) and twist-escaped disclination loop (red line in the schematic midplane) that conserve the total topological charge of structures embedded into a uniform vertical far-field director. (B) vertical xz computer simulated cross-section of **n(r)** with two blue dots (top and bottom) marking the hyperbolic point defects and two red dots (on the left and right sides of the schematic) marking the intersection of the disclination loop with the cross-section. (C,D) Computer simulated (C) and experimental (D) 3PEF-PM textures of a laser generated toron in a 5μm thick cell visualized using the Paraview software for sample volumes of high intensity signal representing azimuthal and polar deviations of the director away from vertical and towards the direction of probing 3PEF-PM polarization [48]. The intensity threshold was adjusted to show a continuous 3D representation of the director's in-plane orientation for which four experimental data sets (corresponding to four different polarizations of 3PEF-PM excitation light) were used. The different colors (gray scale levels) visualize sample regions yielding high intensity of 3PEF-PM signal when imaged using different azimuthal orientations of linear polarization of the 3PEF-PM laser excitation light (as depicted in the inset for four angles that the linear 3PEF-PM polarization makes with the x-axis). The lateral size of the toron shown in (D) is about 5μm. (E) Vector-field representation of the axially-symmetric toron structure that yield the two point defects having opposite hedgehog charges and the rest of the three-dimensional texture having zero hedgehog charge. For the selected direction of vector field (arrows) at the global point of reference (chosen to be the point defect at the bottom part of the structure) in (E), the hyperbolic hedgehog of "+1" charge is marked by a yellow filled circle (bottom part of the schematic) while the defect of "-1" charge is marked by a blue filled circle (top part of the schematic). The white filled circles indicate the location of the axis of the looped double twist cylinder intersecting the schematic (E) in its midplane. Note that (due to nonpolar symmetry of the director) the choice of the vector directions is arbitrary and that the signs of

both of the hyperbolic point defects can be reversed by changing the direction of arrows in the vector field.

Fig. 5. (Color online). Periodic arrays of torons as voltage-tunable phase gratings. POM textures of (A) square and (B) hexagonal periodic arrays of laser generated torons with the insets showing the corresponding diffraction patterns obtained using a 633nm HeNe laser. Thin lines in-between the beams of the same diffraction orders shown in (B) are used for eye guiding and have colors (grey scale levels) matched to the colors (grey scale levels) of corresponding data points presented in (D). (C) Horizontal intensity profile of the square periodic diffraction pattern along the C-C line marked on (A). (D) Intensity of light in the hexagonal diffraction pattern vs. applied voltage across the cell with the phase grating of torons for different diffraction orders. The crossed polarizer and analyzer are shown by blue double arrows and marked by "P" and "A", respectively.

Fig. 6. (Color online). Hexagonal periodic arrays of torons as voltage-tunable phase gratings. (A-F) POM textures of square periodic arrays of laser-generated torons with the insets showing corresponding diffraction patterns obtained using a circularly polarized 633nm HeNe laser; the applied voltages are marked in the bottom left corners of the images. The crossed polarizer and analyzer are shown by white double arrows and marked by "P" and "A", respectively.

Fig. 7. (Color online). Square periodic arrays of torons as voltage-tunable phase diffraction gratings. (A-F) POM textures of square periodic arrays of laser-generated torons with the insets showing corresponding diffraction patterns obtained with a 633nm circularly polarized HeNe laser. The orientation of crossed polarizer and analyzer at all voltages is shown in (D) by use of blue double arrows marked by "P" and "A", respectively.

Fig. 8. (Color online). Computer-simulated diffraction patterns obtained for (A) square-periodic and (B) hexagonal arrays of torons.

Fig. 9. (Color online). Control of phase singularities by defects in toron gratings. (A) POM texture of a square-periodic array of torons with an edge dislocation labeled by a red arrow

(located near the center of image) and (B) a corresponding diffraction pattern with diffraction orders marked on the image and a large-area view containing higher diffraction order beams shown in the inset. (C) An enlarged image of the first-order diffracted beam and (D) an interference pattern of the first-order diffraction and reference Gaussian beams obtained for their oblique incidence. (E) Phase profile of the first-order beam shown in (C). (F) An enlarged image of a second-order diffracted beam and (G) interference pattern of this beam and a reference Gaussian beam obtained for their oblique incidence. (H) Phase profile of the second-order beam shown in (F). 3D plots of the phase vs. coordinates in the lateral plane of the diffracted beams of first (I) and second (J) orders, respectively, with green vertical lines showing locations of the phase singularities. The orientation of crossed polarizer and analyzer in (A) is shown by use of blue double arrows marked by "P" and "A", respectively.

Fig. 10. (Color online). Hexagonal arrays of torons with defects and the corresponding diffraction patterns with phase singularities. (A,B) POM textures of hexagonal periodic array of torons with dislocations at applied voltages of (A) U=0 and (B) U=0.8 V_{p-p}. The inset of (B) shows the 5-7 defects in the hexagonal toron array by means of a Voronoi diagram. (C) Diffraction pattern obtained using a grating shown in (A). (D,E) Phase profiles of the first-order diffraction beams marked in (C). The orientation of crossed polarizer and analyzer in POM textures is shown in (A) by use of blue double arrows marked by "P" and "A", respectively.
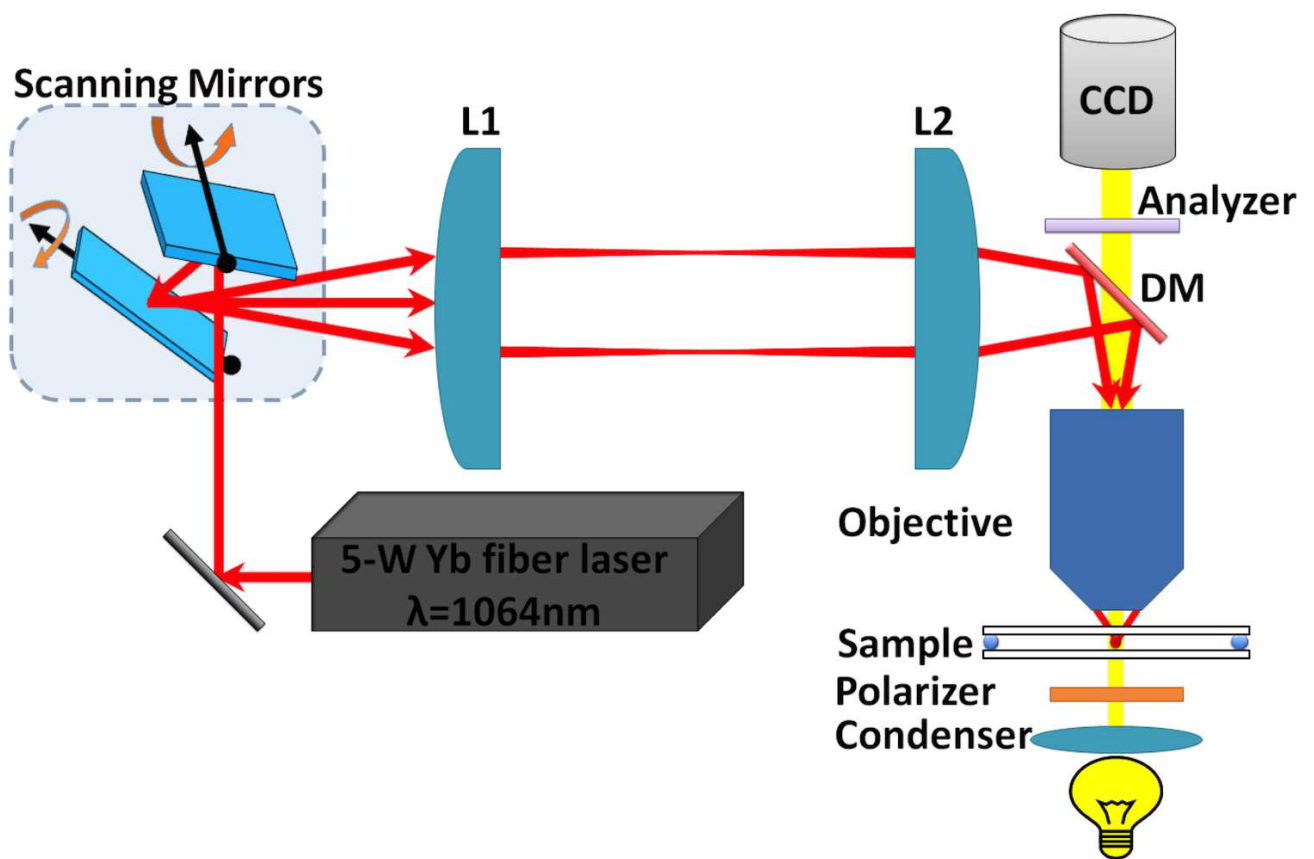
Fig. 11. (Color online). Square-periodic array of torons with defects and the corresponding diffraction pattern. (A) POM texture of the array and the corresponding diffraction pattern shown in the inset obtained for a 633nm HeNe laser; the two diffracted beams in different diffraction orders are marked in the inset as m_x=1, m_y=0 and m_x=1, m_y=1. (B) Phase profile (top) and an interference pattern of the m_x=1, m_y=0 diffraction beam and a reference Gaussian beam obtained for their oblique incidence (bottom). (C) A 3D representation of the phase vs. coordinates in the lateral plane of the diffracted beam of the m_x=1, m_y=0 diffraction order. (D) Phase profile (top) and an interference pattern (bottom) of the m_x=1, m_y=1 diffraction order beam and a reference Gaussian beam obtained for their oblique incidence (bottom). (E) A 3D representation of the phase vs. coordinates pattern in the lateral plane of the diffracted beams of the m_x=1, m_y=1

diffraction order beam. (F-H) Computer simulation of intensity (F) and phase distribution (G) of the diffraction pattern plotted separately (F,G) and then overlaid on top of each other (H). The orientation of crossed polarizer and analyzer in (A) is shown by use of blue double arrows marked by "P" and "A", respectively.

Fig. 12. (Color online). Computer-simulated (A,D) intensity and (B,E) phase distributions for diffraction gratings that correspond to the experimental counterparts shown in Fig. 10 and Fig 9, respectively. (C,F) Overlaid plots of lateral intensity and phase distributions of the diffraction patterns obtained by superimposing parts (A) with (B) and (D) with (E), respectively.

Fig. 13. (Color online). Square periodic arrays of torons with defects as voltage-tunable phase gratings. (A-D) POM textures of square periodic arrays of laser generated torons at different applied voltages (marked on the images) with the insets showing corresponding diffraction patterns obtained with a 633nm HeNe laser. The orientation of crossed polarizer and analyzer in the POM textures is shown in (C) by use of blue double arrows marked by "P" and "A", respectively.

Fig. 14. (Color online). POM images of (A) a honeycomb lattice of torons and (B) a square-periodic array of torons with a bifurcated homeotropic channel. The orientation of crossed polarizer and analyzer in these POM textures is shown by use of blue double arrows marked by "P" and "A", respectively.

Fig. 15. (Color online). (A-C) POM images of laser-generated quasicrystal-like structures of torons obtained by mimicking quasicrystal structures described in Ref. [50]. The lateral size of torons is about 10μm in all POM images. The orientation of crossed polarizer and analyzer in the POM textures is shown by use of blue double arrows marked by "P" and "A", respectively.

Scanning Mirrors

L1

L2

CCD

Analyzer

DM

Objective

Sample

Polarizer

Condenser

5-W Yb fiber laser
λ=1064nm

Figure 1   ET10802   04AUG12
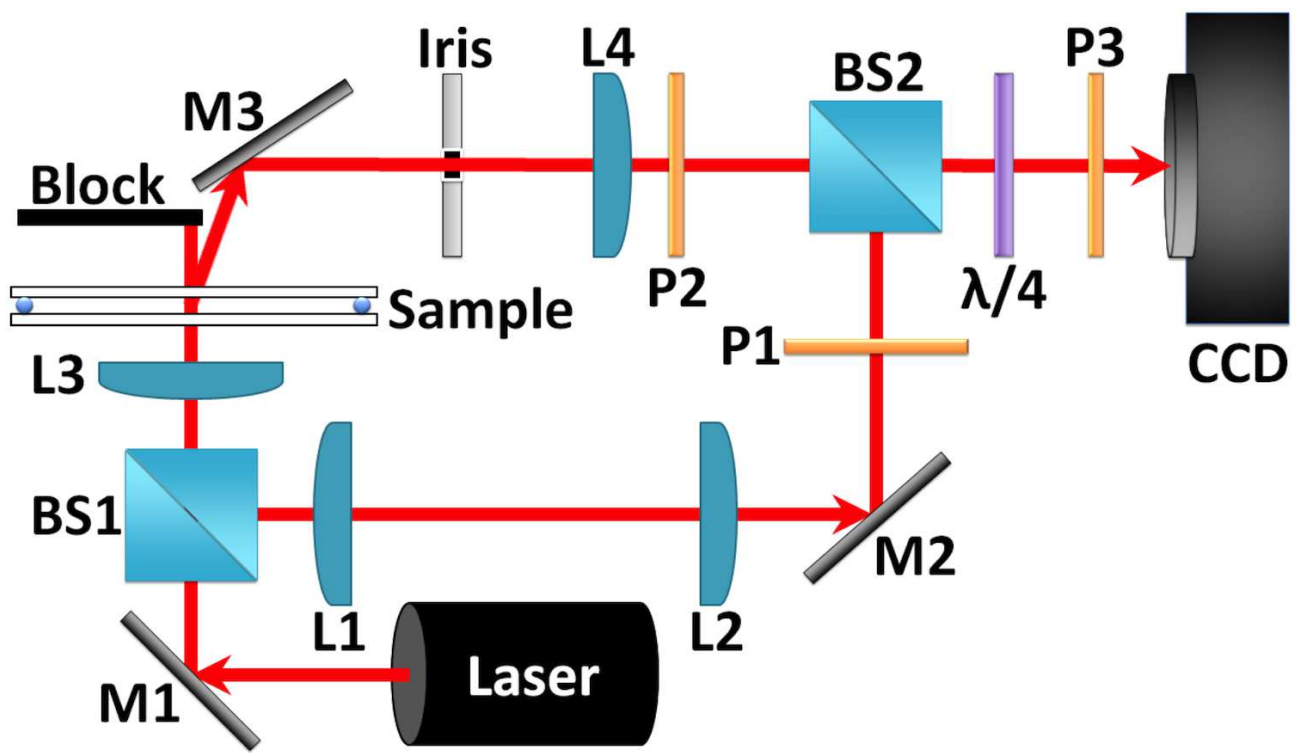
Figure 2   ET10802   04AUG12
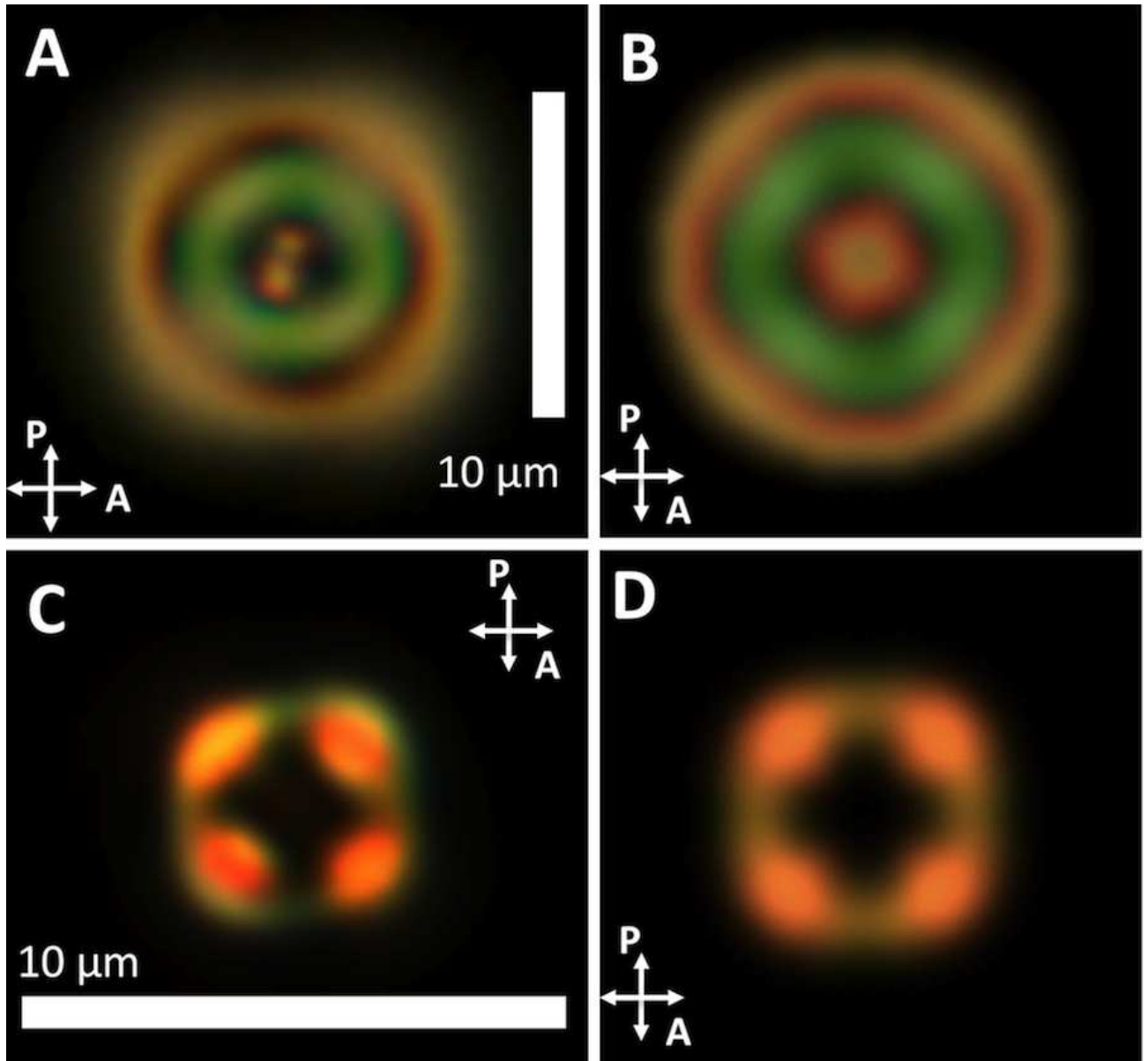
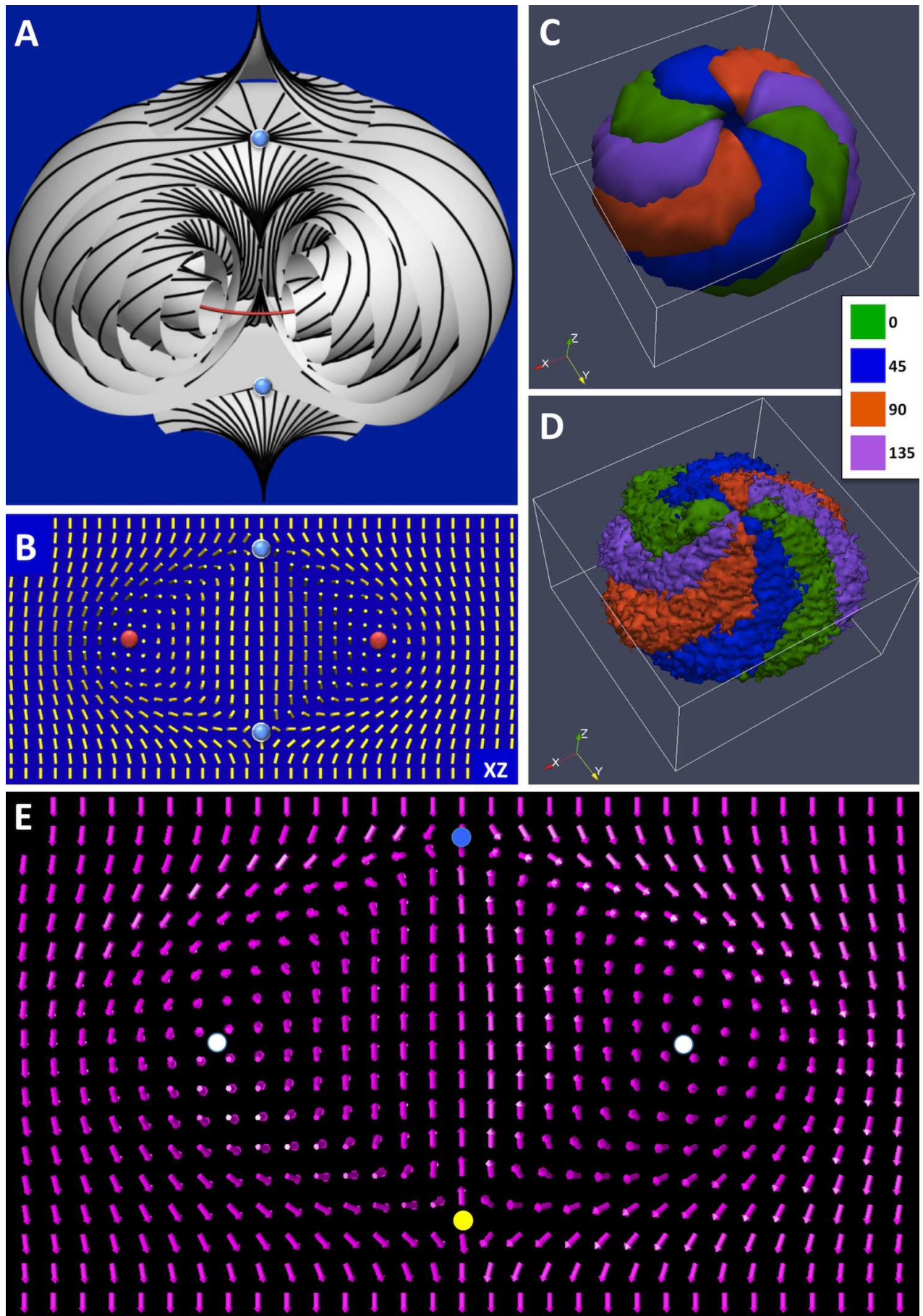Figure 3   ET10802   04AUG12

Figure 4   ET10802   04AUG12
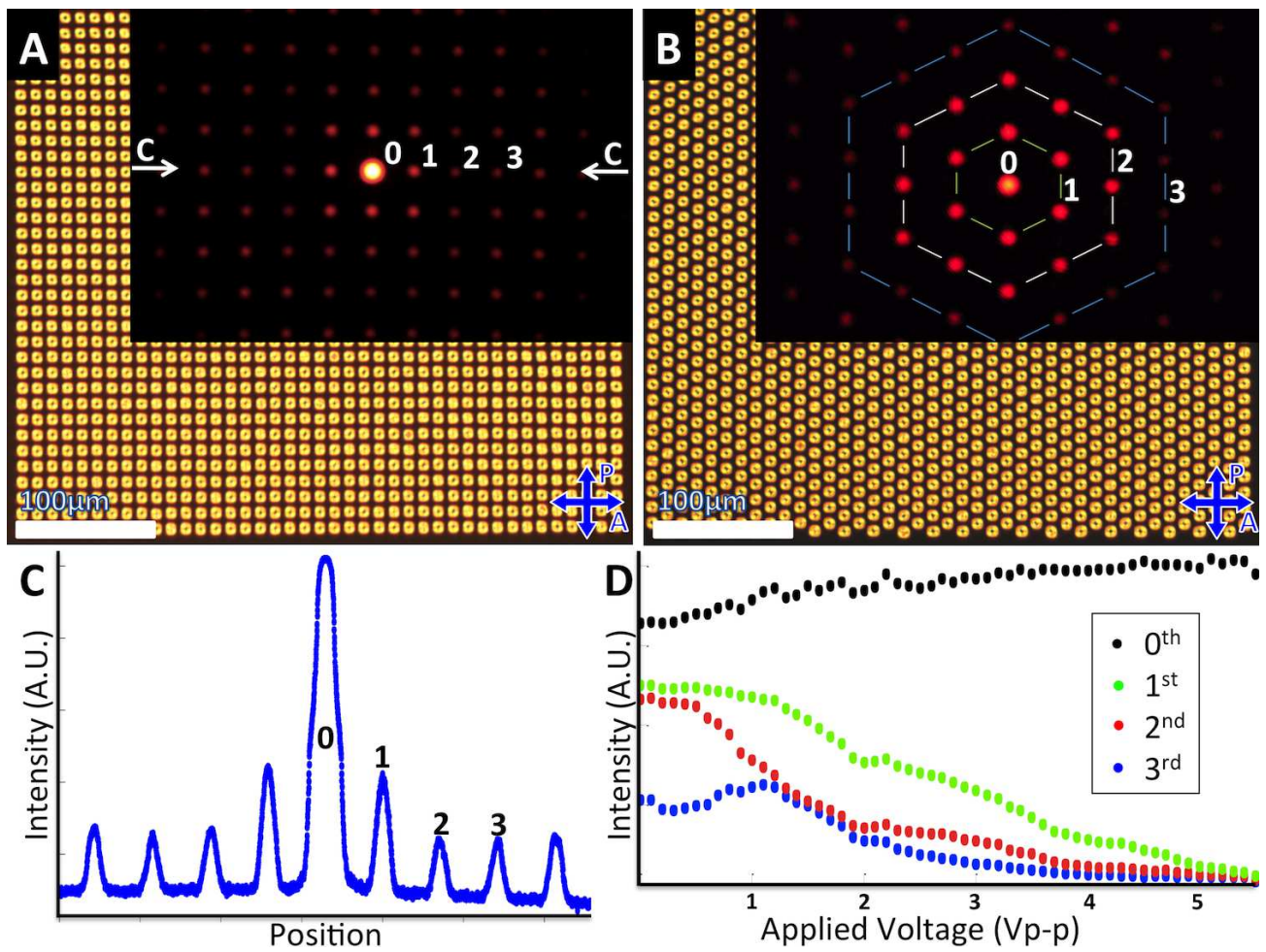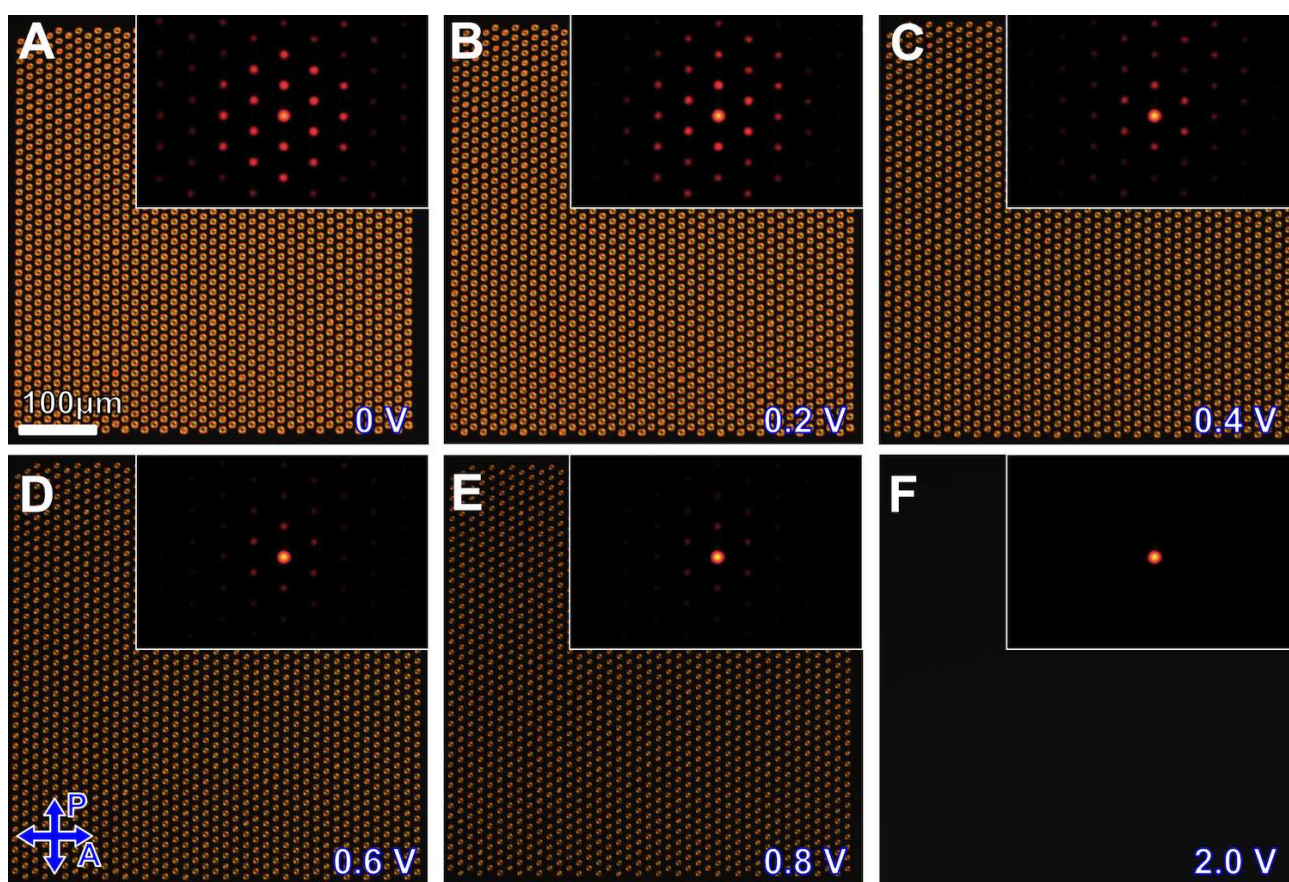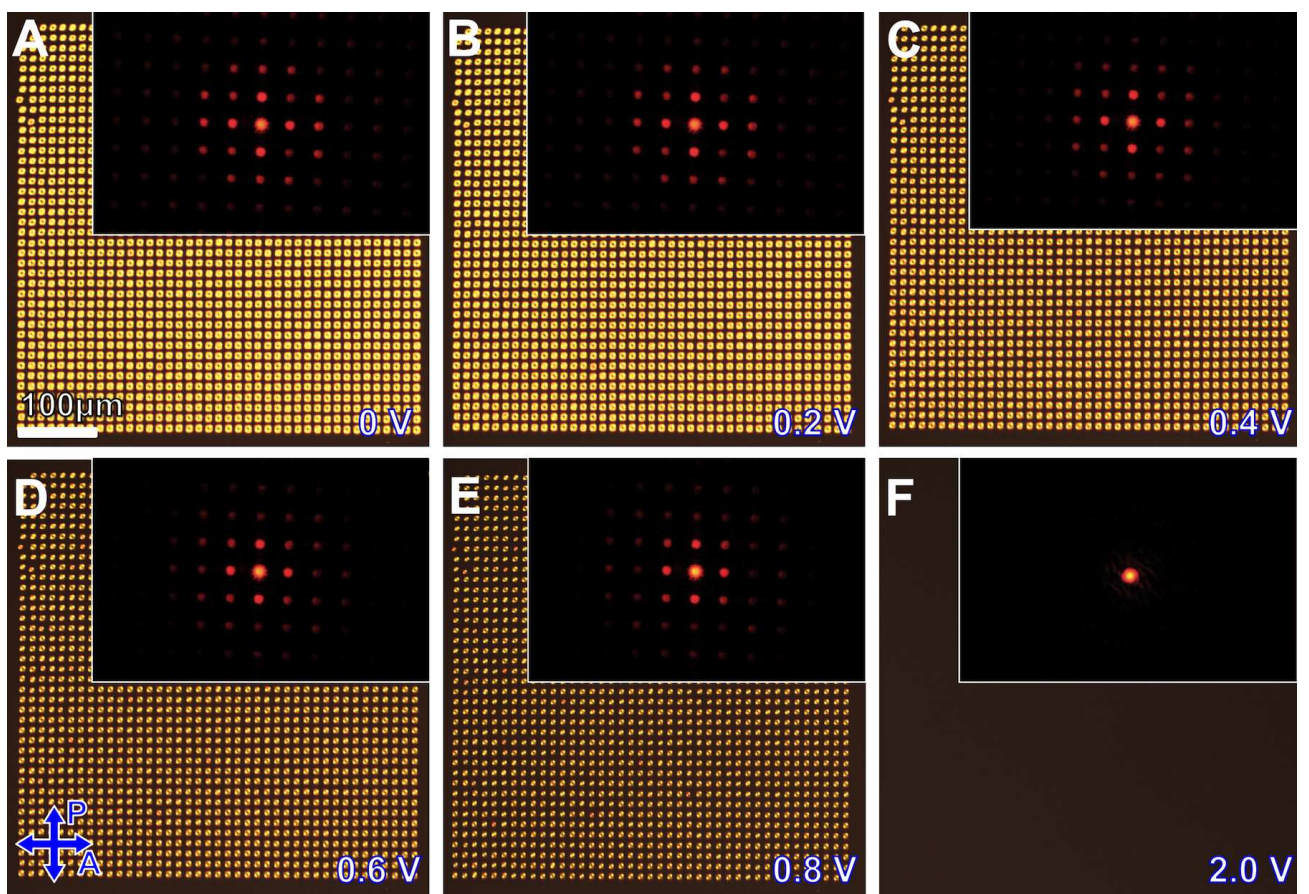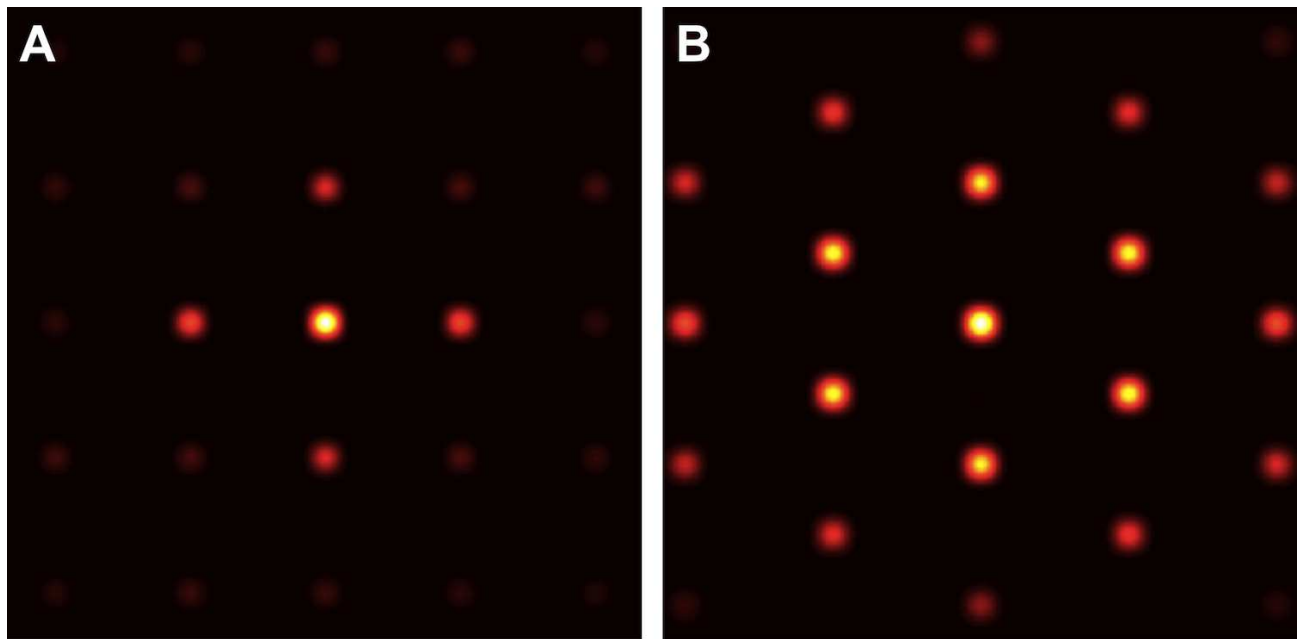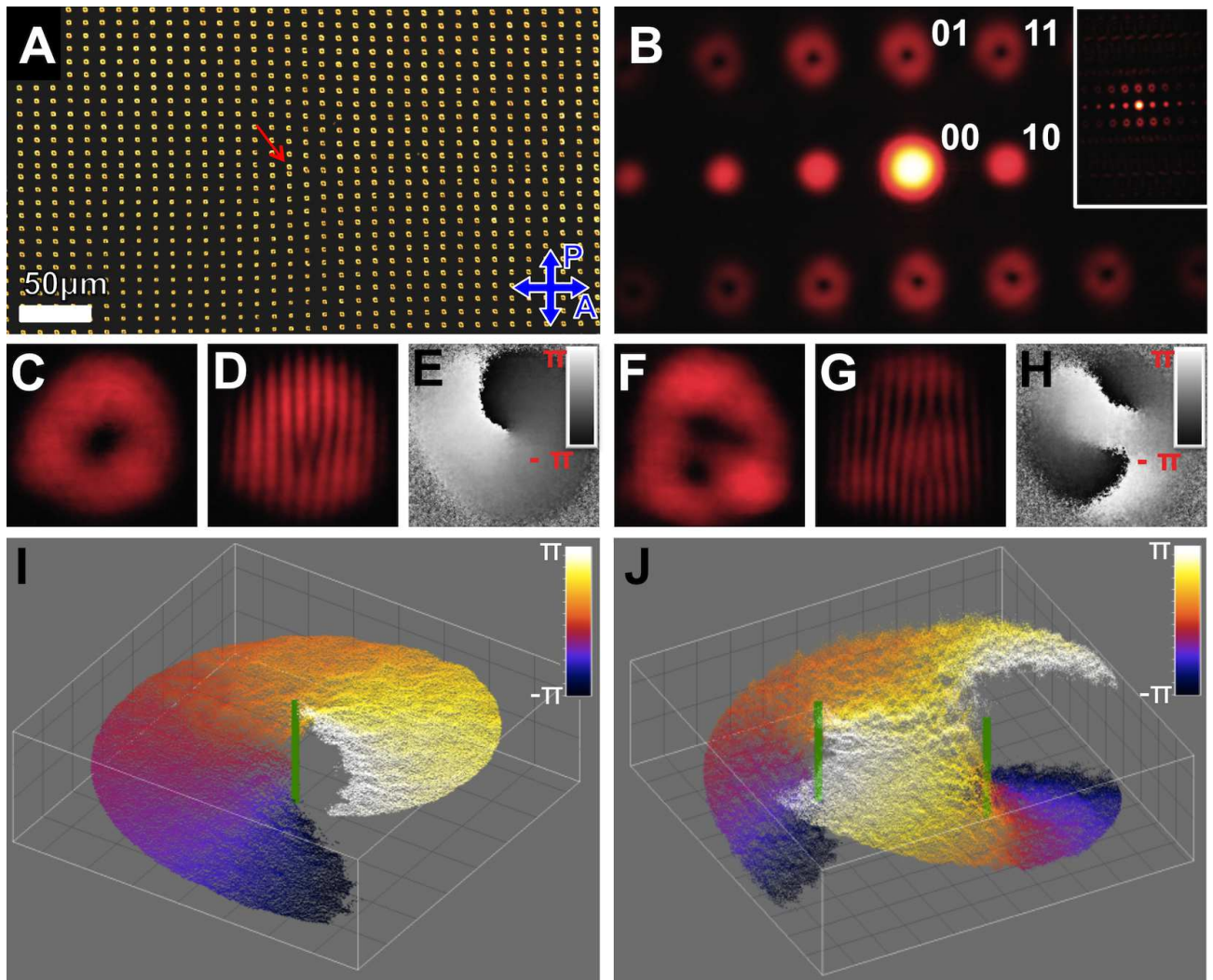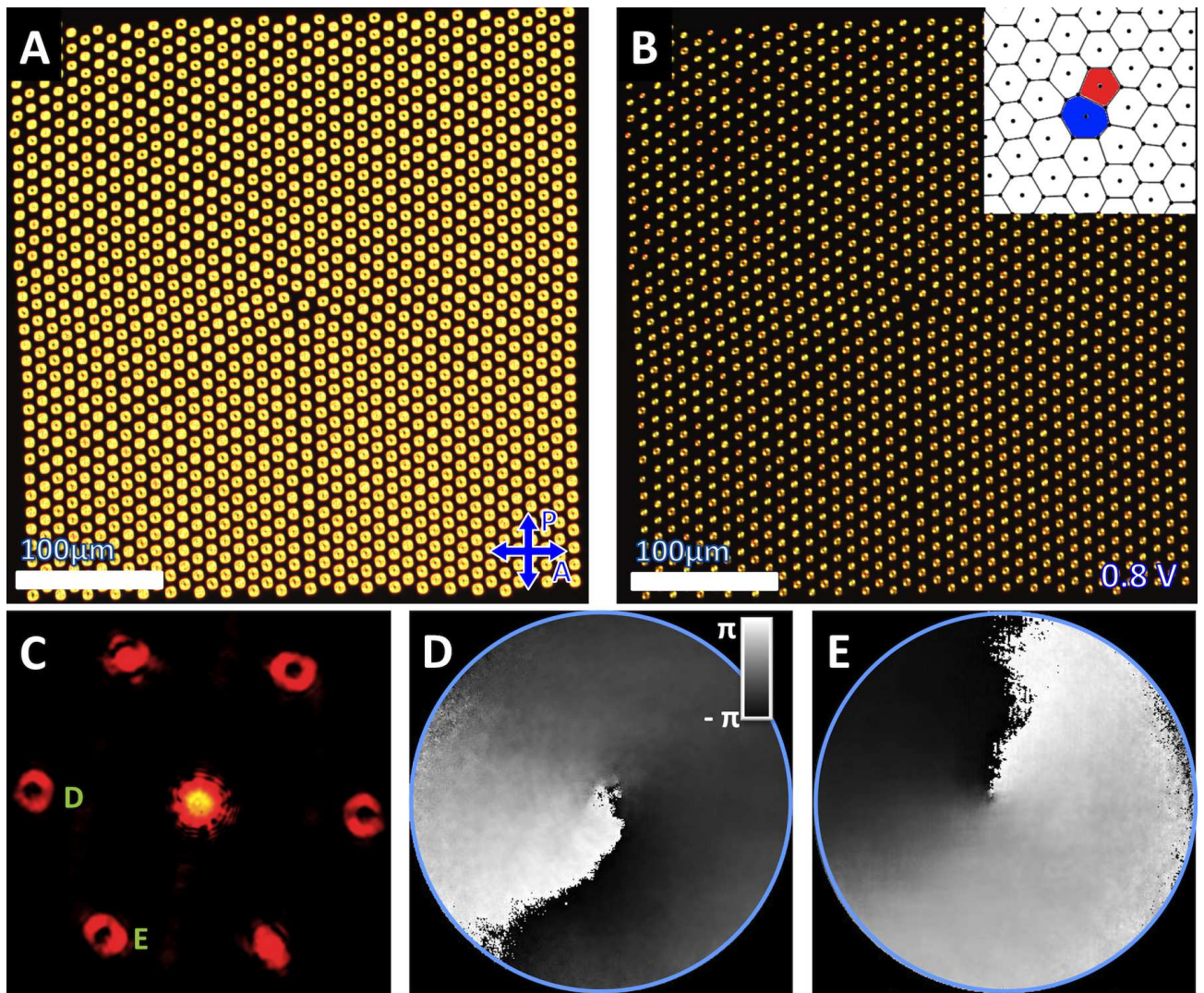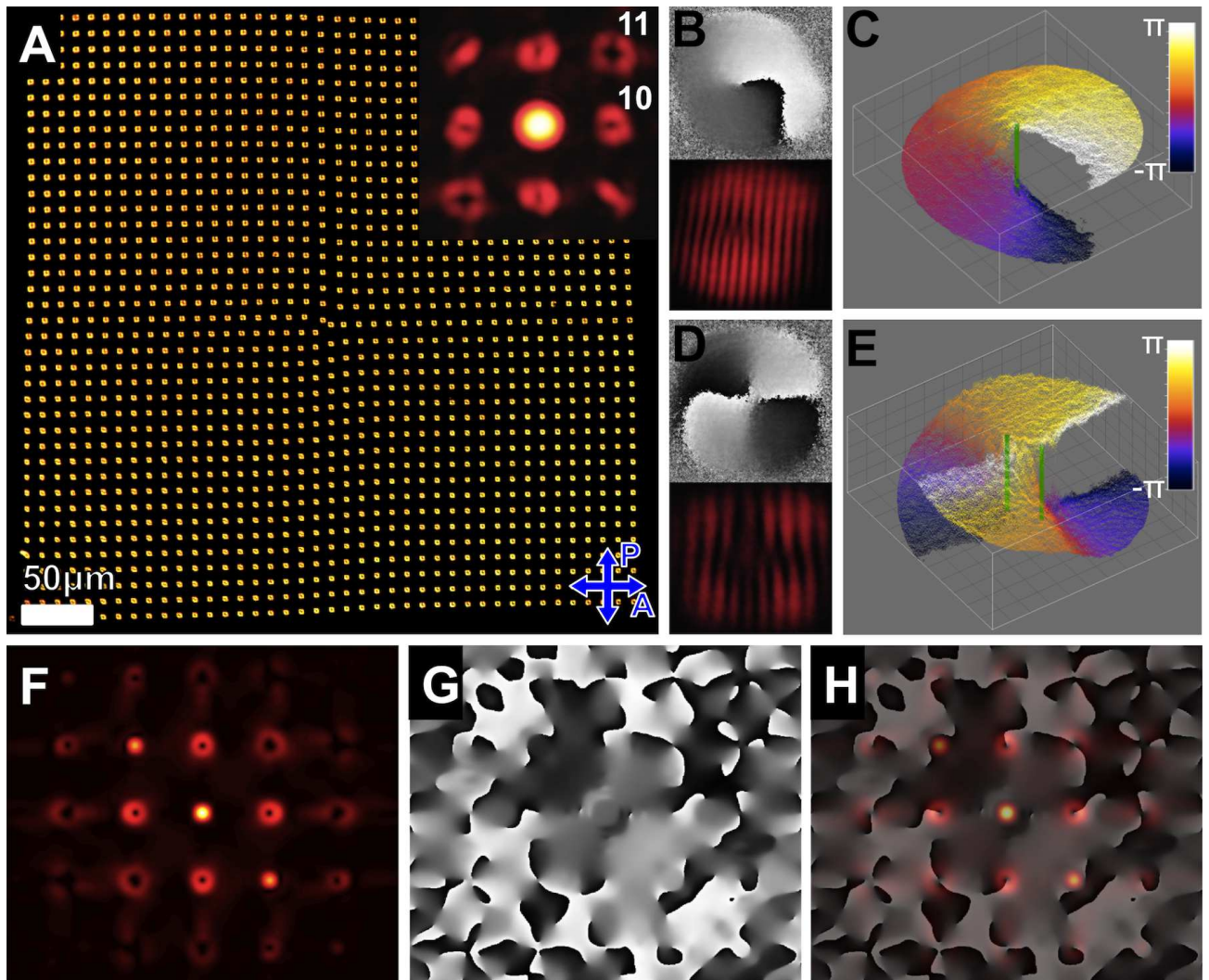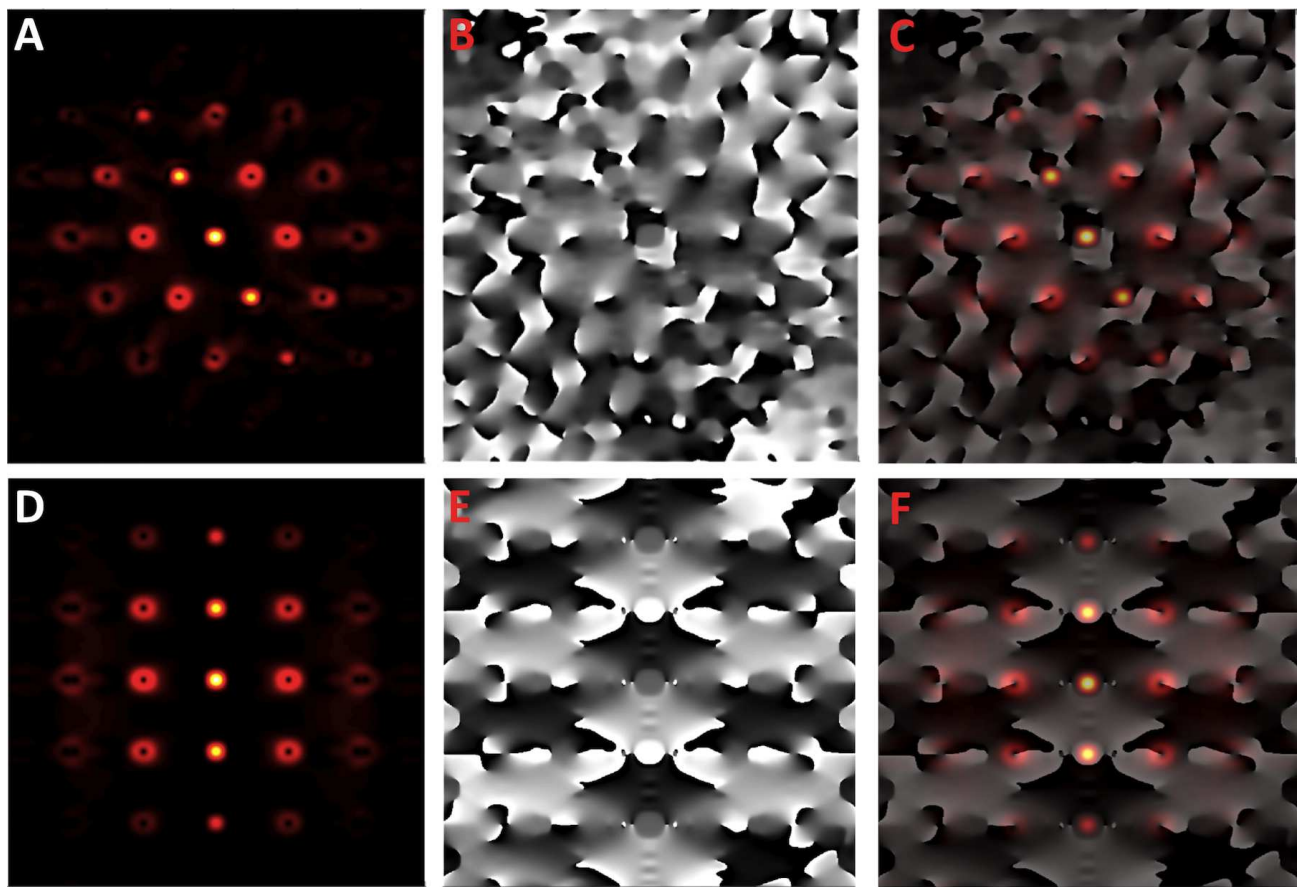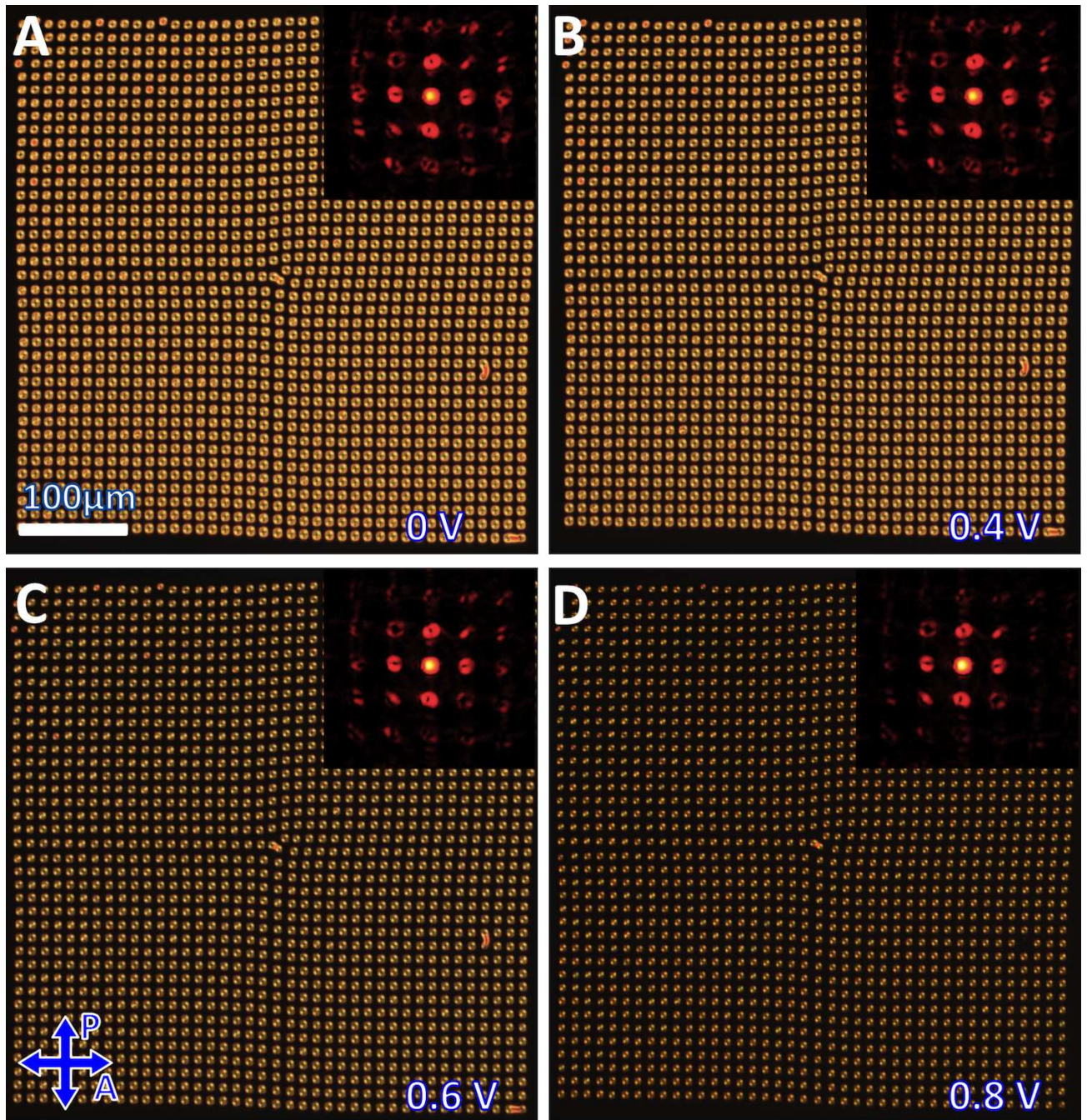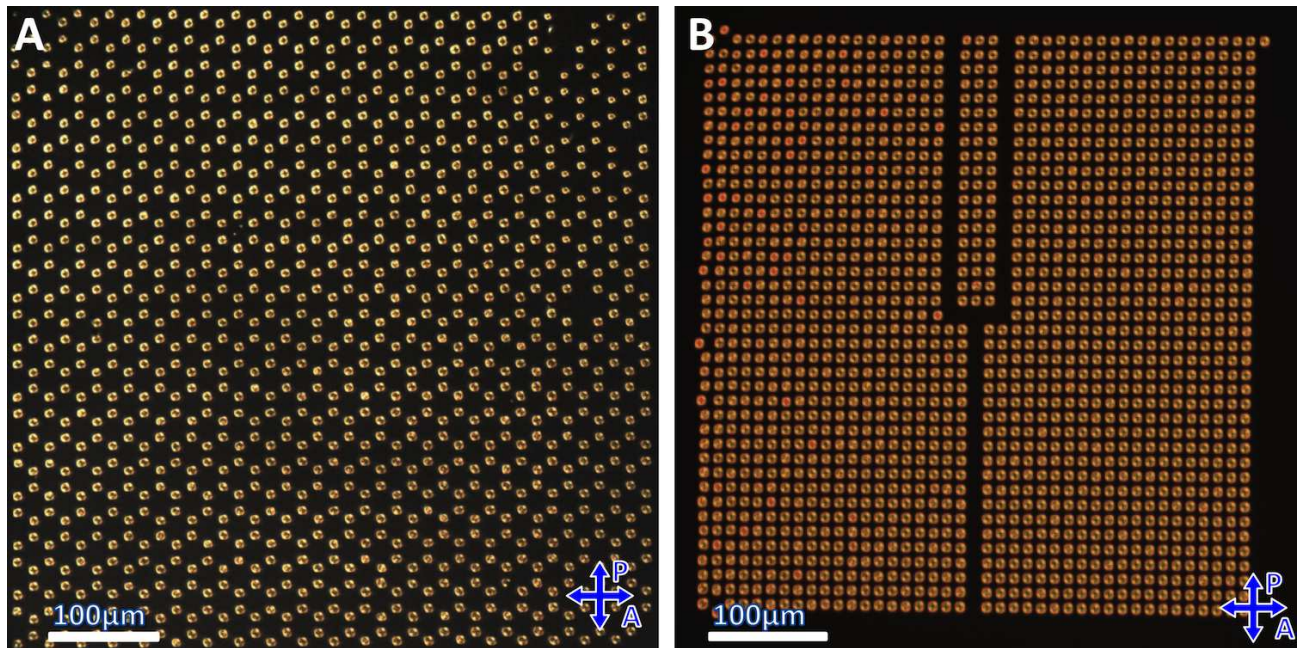
Figure 5   ET10802   04AUG12

Figure 6   ET10802   04AUG12

Figure 7   ET10802   04AUG12

Figure 8   ET10802   04AUG12

A

01 11

00 10

B

C   D   E   π / -π

F   G   H   π / -π

I   π / -π

J   π / -π

50μm

P
A

Figure 9   ET10802   04AUG12

Figure 10   ET10802   04AUG12

Figure 11   ET10802   04AUG12

Figure 12   ET10802   04AUG12
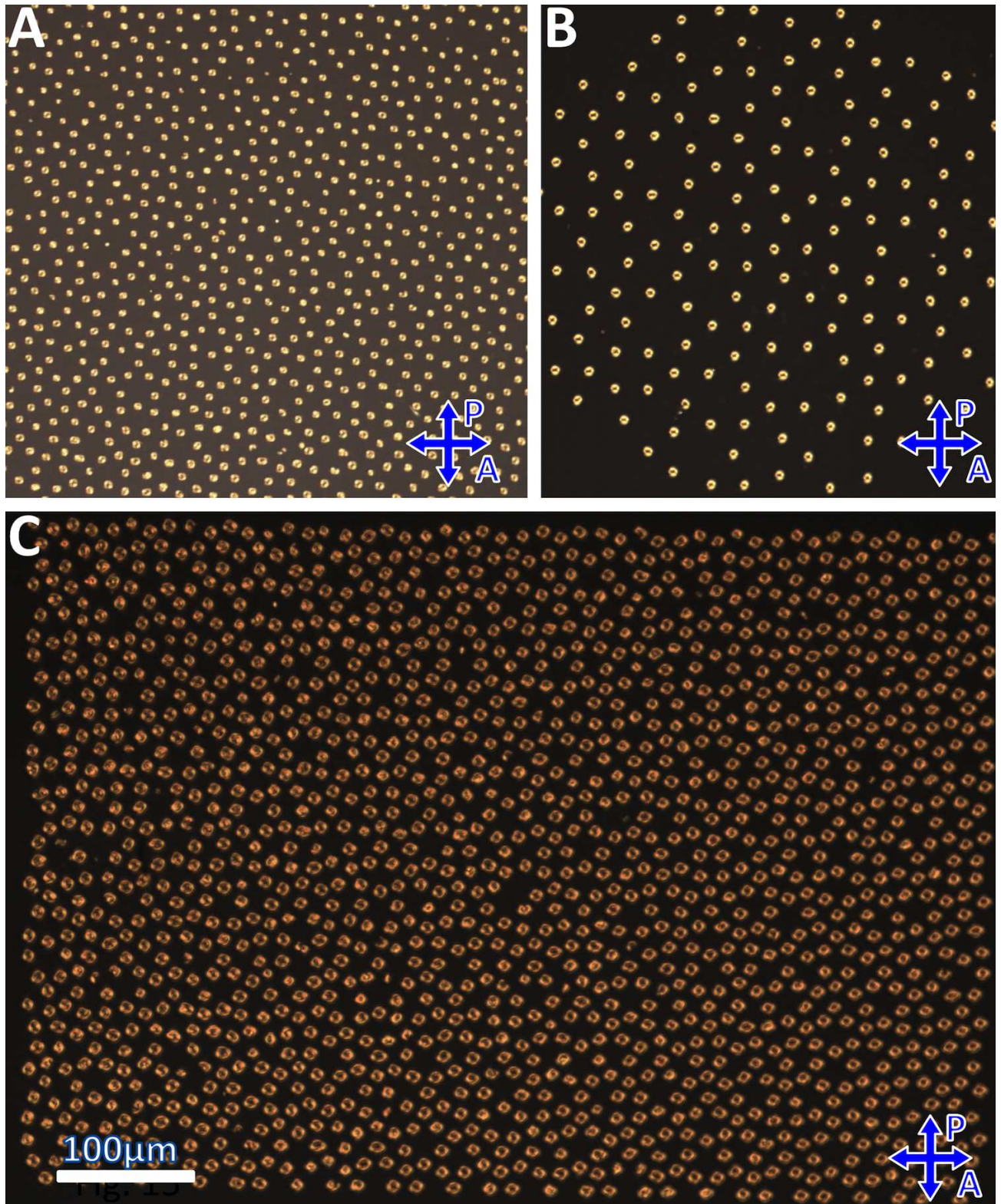
Figure 13　　　ET10802　　04AUG12

Figure 14   ET10802   04AUG12

Figure 15   ET10802   04AUG12